



# Long-term ozone formation sensitivity in China: spatiotemporal evolution and machine learning attribution

Jinglan Lin<sup>1</sup>, Liqing Wu<sup>2</sup>, Chujun Chen<sup>1</sup>, Yongkang Wu<sup>1</sup>, Rui Lin<sup>3</sup>, Xuemei Wang<sup>1</sup>, and Weihua Chen<sup>1</sup>

<sup>1</sup>College of Environment and Climate, Jinan University, Guangzhou, 510632, PR China

<sup>2</sup>College of Ocean and Meteorology, Guangdong Ocean University, Zhanjiang, 524000, PR China

<sup>3</sup>High Performance Computing Department, National Supercomputing Center in Shenzhen, Shenzhen, 518000, PR China

**Correspondence:** Weihua Chen (chenwh26@jnu.edu.cn)

Received: 19 November 2025 – Discussion started: 17 December 2025

Revised: 13 April 2026 – Accepted: 5 May 2026 – Published: 22 May 2026

**Abstract.** Accurate diagnosis of ozone ( $O_3$ ) formation sensitivity (OFS) is essential for designing effective precursor-control strategies, yet long-term, observation-based, and interpretable national-scale assessments remain limited. Here, we combined OMI satellite observations of tropospheric nitrogen dioxide ( $NO_2$ ) and formaldehyde (HCHO) with ground-based  $O_3$  measurements to derive region-specific FNR ( $HCHO/NO_2$ ) threshold ranges from the relationship between FNR and  $O_3$  exceedance probability. Based on these thresholds, we characterized the spatiotemporal evolution of OFS across China during the warm season (April–September) from 2005 to 2023 and coupled Random Forest (RF) with SHapley Additive exPlanations (SHAP) to quantify contributions from emission-related and meteorological factors. The results reveal a clear phase reversal in OFS over China. From 2005 to 2012, the national area fraction of nitrogen oxides ( $NO_x$ )-limited regimes decreased by 7.9 %, while transitional and volatile organic compound (VOC)-limited regimes increased by 5.6 % and 2.3 %, respectively. After 2013, this pattern reversed, and by 2023  $NO_x$ -limited regimes expanded to 76.5 % of the polluted area, whereas VOC-limited regimes accounted for only 2.8 %. Regionally, after 2013, both Beijing–Tianjin–Hebei (BTH) and Fenwei Plain (FWP) exhibited transitions between transitional and  $NO_x$ -limited regimes, while the Yangtze River Delta (YRD) showed a shift toward  $NO_x$ -limited regimes. Sichuan Basin (SCB) remained predominantly transitional, and Pearl River Delta (PRD) also shifted toward  $NO_x$ -limited regimes. SHAP analysis shows emission-related variables contributed 50.1 %–69.4 % of total importance, exceeding meteorological factors, which increased after 2013. Overall, OFS evolution is primarily associated with emission changes but increasingly modulated by meteorological conditions under cleaner conditions.

## 1 Introduction

Over the past decade, China has enacted a series of unprecedented clean air policies, most notably the “Air Pollution Prevention and Control Action Plan (2013–2017)” (Chinese State Council, 2013) and the “Three-Year Action Plan for Winning the Blue Sky Defense Battle (2018–2020)” (Chinese State Council, 2018). These coordinated efforts have successfully driven substantial declines in fine particulate matter ( $PM_{2.5}$ ), yielding a stagewise improvement in national

air quality (Geng et al., 2024; Liu et al., 2024). However, surface ozone ( $O_3$ ) levels have concurrently risen across major urban clusters (Li et al., 2020; Wang et al., 2022; Wei et al., 2022). This upward trend has established  $O_3$  as the primary obstacle to further air quality gains in the post- $PM_{2.5}$  era, making China one of the regions most severely affected by  $O_3$  pollution globally (Lu et al., 2018). Persistent elevations in  $O_3$  concentrations are particularly evident in Beijing–Tianjin–Hebei (BTH), the Yangtze River Delta (YRD), the Pearl River Delta (PRD), the Fenwei Plain

(FWP), and the Sichuan Basin (SCB) (Chen et al., 2021; Guan et al., 2021; Deng et al., 2022; Hu et al., 2024), posing documented risks to public health and ecosystem productivity (Lin et al., 2018; Liang et al., 2024a; Hua et al., 2025).

The complexity of O<sub>3</sub> mitigation stems from its nature as a secondary pollutant, formed through nonlinear photochemical reactions involving nitrogen oxides (NO<sub>x</sub> = NO + NO<sub>2</sub>) and volatile organic compounds (VOCs) (Seinfeld and Pandis, 2016). This nonlinearity implies that O<sub>3</sub> responses to precursor reductions vary significantly across different chemical regimes and meteorological conditions. O<sub>3</sub> formation sensitivity (OFS) is thus typically classified into NO<sub>x</sub>-limited, VOC-limited, and transitional regimes (Kleinman, 1994; Sillman, 1999; Martin et al., 2004; Duncan et al., 2010; Schroeder et al., 2017). Consequently, a reliable and regionally appropriate classification of OFS regimes, together with a clear attribution of their controlling factors, is essential for developing effective, region-specific multi-pollutant control strategies.

Methods for diagnosing OFS have evolved into two primary categories: model-based and observation-based approaches (Liu and Shi, 2021). Model-based approaches mainly include source tagging techniques and sensitivity experiments within chemical transport models. Source tagging techniques determine O<sub>3</sub> formation regimes by tracking the contributions of precursor species, such as NO<sub>x</sub> and VOCs, in air quality models. For instance, Wu et al. (2022) applied the Community Multiscale Air Quality (CMAQ) model coupled with the O<sub>3</sub> Source Apportionment Technology (OSAT) and showed that OFS in the PRD region varied substantially under different meteorological conditions. Sensitivity experiments, by contrast, estimate O<sub>3</sub> response to precursor emission perturbations using models such as WRF-Chem and GEOS-Chem. Using an Observation-Based Model (OBM) coupled with the WRF-CMAQ model, Zhang et al. (2024c) demonstrated dynamic shifts in northeastern China from VOC-limited or transitional regimes to NO<sub>x</sub>-limited regimes as pollution intensifies. Although these approaches provide valuable process-level insight, they are computationally demanding and depend strongly on model performance, which limits their broad applications, especially for long-term and large-scale assessments.

Against this background, observation-based photochemical indicators provide a simpler and more efficient alternative for OFS diagnosis and regional mapping. These methods infer O<sub>3</sub> formation regimes from the ratios of chemically relevant species. Milford et al. (1994) initially proposed total reactive nitrogen (NO<sub>y</sub> = NO<sub>x</sub> + nitric acid [HNO<sub>3</sub>] + peroxyacetyl nitrates + alkyl nitrates) as a diagnostic indicator, which was subsequently extended to indicators such as hydrogen peroxide (H<sub>2</sub>O<sub>2</sub>) / HNO<sub>3</sub>, O<sub>3</sub> / NO<sub>x</sub>, and formaldehyde (HCHO) / NO<sub>y</sub> ratios (Sillman, 1995; Tonnesen and Dennis, 2000). Among these, the satellite-based ratio of HCHO to nitrogen dioxide (NO<sub>2</sub>), commonly referred to as FNR, has received increasing attention because

of its broad spatial coverage, continuous temporal record, and strong regional representativeness (Chen et al., 2023; Li et al., 2024; Vazquez Santiago et al., 2024).

A key issue in applying FNR is the determination of appropriate threshold values for OFS classification. Duncan et al. (2010) proposed a threshold range for the United States using air quality models, a photochemical box model, and OMI-derived HCHO and NO<sub>2</sub> data. This range has since been widely adopted in OFS studies in China (Jin and Holloway, 2015; Itahashi et al., 2022). However, later studies showed that FNR thresholds are not universal. Schroeder et al. (2017) pointed out that regional differences, stratospheric contributions, and satellite retrieval uncertainties can all affect threshold values. Zhang et al. (2024b) further reported that FNR thresholds can also vary across time scales. These findings suggest that the commonly used fixed range of [1, 2] may not be suitable for China, where precursor emissions, atmospheric environments, and meteorological conditions vary substantially across regions. Applying a uniform threshold may therefore introduce biases in OFS diagnosis.

Given these limitations, increasing efforts have been made to derive regionally appropriate FNR thresholds by combining satellite HCHO / NO<sub>2</sub> observations with surface O<sub>3</sub> measurements in different parts of China (Song et al., 2023; Chen et al., 2024; Li et al., 2024). For example, Ren et al. (2022) analyzed data from April to September during 2019–2021 and found that the national-scale FNR threshold was around [2.2, 3.2], whereas regional thresholds ranged from about [1.2, 3.2] to [3.2, 4.3]. This large range highlights substantial regional heterogeneity in OFS. Building on these studies, a more systematic evaluation of FNR thresholds across China's major city clusters is still needed to provide more reliable region-specific criteria for OFS diagnosis.

Beyond threshold determination, understanding the long-term evolution of OFS and its influencing factors is equally important. Previous studies have shown that OFS in many parts of China has shifted over the past two decades from VOC-limited regimes toward NO<sub>x</sub>-limited or transitional regimes (Du et al., 2022; Itahashi et al., 2022; Johnson et al., 2024). This shift reflects not only changes in precursor emissions, but also the influence of meteorological variability and climate change (Zhan et al., 2022; Badia et al., 2023). Under continued climate warming, more frequent heat extremes and enhanced shortwave radiation may further alter the spatial patterns and long-term evolution of OFS (Vazquez Santiago et al., 2024). However, an understanding of how emissions and meteorology reshape OFS remains limited, particularly at the national scale and over multi-decadal periods.

To address these gaps, this study combines OMI satellite observations of tropospheric NO<sub>2</sub> and HCHO from 2005 to 2023 to characterize the spatiotemporal evolution of O<sub>3</sub> precursors and OFS across China during the warm season (April–September), with explicit comparison of the periods before and after major air quality policies (2005–2012 vs.

2013–2023). Rather than proposing a fundamentally new OFS diagnostic framework, we derive region-specific FNR threshold ranges for different regions of China based on satellite observations and surface  $O_3$  data and use these thresholds to classify OFS regimes. We further couple a Random Forest (RF) model with SHapley Additive exPlanations (SHAP) to statistically characterize how meteorological and emission-related factors are associated with the occurrence and long-term evolution of the FNR-derived OFS states. In this framework, OFS is diagnosed using the satellite-based FNR indicator, whereas the machine learning analysis is used for driver attribution rather than to diagnose OFS directly. This framework provides a more regionally appropriate basis for OFS classification in China and offers an interpretable perspective on the relative roles of emissions and meteorology in OFS evolution.

## 2 Data and methods

### 2.1 Study area and data sources

#### 2.1.1 Study area

This study focuses on mainland China and five major urban clusters with severe  $O_3$  pollution, namely the Beijing–Tianjin–Hebei (BTH) region, the Yangtze River Delta (YRD), the Fenwei Plain (FWP), the Pearl River Delta (PRD), and the Sichuan Basin (SCB) (Fig. 1). These regions were selected because they have persistently high  $O_3$  levels and are widely recognized as major  $O_3$  pollution hotspots in China (Ozone Pollution Control Committee of Chinese Society of Environmental Sciences, 2024). They also represent distinct combinations of emission characteristics, meteorological conditions, and topographic settings, making them suitable for examining the regional heterogeneity of OFS (Wang et al., 2017; Zhang et al., 2025b).

#### 2.1.2 Satellite data

$NO_x$  has a short lifetime in the boundary layer, and NO is rapidly converted to  $NO_2$ . Therefore, the  $NO_2$  column is commonly used as a proxy for ambient  $NO_x$  levels (Duncan et al., 2010). HCHO is a major intermediate product of VOCs oxidation, with a relatively short lifetime and a dominant distribution in the troposphere, making its total column abundance a useful indicator of tropospheric VOCs (Duncan et al., 2010).

In this study, daily  $NO_2$  and HCHO column data from 2005 to 2023 were obtained from the Ozone Monitoring Instrument (OMI) onboard Aura satellite, available from the National Aeronautics and Space Administration (NASA) Goddard Earth Sciences Data and Information Services Center (<https://disc.gsfc.nasa.gov/>, last access: 6 September 2025). Launched in 2004, OMI provides daily near-global observations with a minimum spatial resolution of approxi-

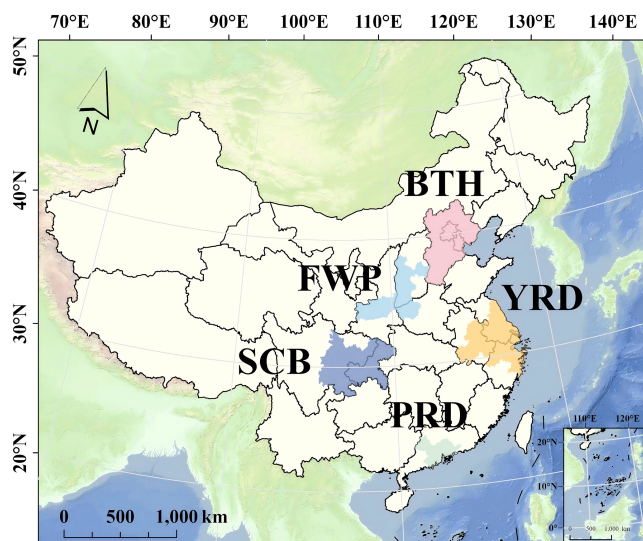


**Figure 1.** Study domain and five key city clusters: Beijing–Tianjin–Hebei (BTH), Fenwei Plain (FWP), Yangtze River Delta (YRD), Sichuan Basin (SCB), and Pearl River Delta (PRD).

mately  $13 \times 24$  km and an overpass time of about 13:45 local time (LT) (Levelt et al., 2006).

Tropospheric  $NO_2$  data were taken from the OMNO2d Level-3 product, which provides daily tropospheric  $NO_2$  columns at a spatial resolution of  $0.25^\circ \times 0.25^\circ$  in units of  $\text{molec. cm}^{-2}$ , and retains only pixels with cloud fraction below 30% (Krotkov et al., 2019). HCHO data were obtained from the Level-3 OMHCHOd product with a spatial resolution of  $0.1^\circ \times 0.1^\circ$  (Chance, 2019). This product is generated based on the Level-2 OMHCHO retrievals after applying quality control filters to exclude pixels with cloud fractions  $> 0.3$ , solar zenith angles  $> 70^\circ$ , or those affected by the OMI row anomaly. The HCHO columns were retrieved using the Smithsonian Astrophysical Observatory (SAO) algorithm, with typical values ranging from  $4 \times 10^{15}$  to  $4 \times 10^{16}$   $\text{molec. cm}^{-2}$  and with a detection limit of approximately  $1.0 \times 10^{16}$   $\text{molec. cm}^{-2}$  (González Abad et al., 2015). Following Zhu et al. (2017), only values between  $-0.5 \times 10^{16}$  and  $1.0 \times 10^{17}$   $\text{molec. cm}^{-2}$  were retained, while values outside this range were treated as outliers and removed. To reduce random noise, a  $3 \times 3$  moving average based on the eight-neighborhood was applied to the HCHO fields. The smoothed HCHO data were then resampled to a  $0.25^\circ \times 0.25^\circ$  grid using bilinear interpolation to match the  $NO_2$  product, following an approach similar to that of Koukouli et al. (2016) for sulfur dioxide ( $SO_2$ ) data.

#### 2.1.3 Meteorological data

Meteorological data for 2005–2023 were obtained from the ERA5 reanalysis dataset produced by the European Centre for Medium-Range Weather Forecasts (ECMWF) (Hersbach

et al., 2020; <https://cds.climate.copernicus.eu/>, last access: 14 September 2025). ERA5 provides monthly data at a spatial resolution of  $0.25^\circ \times 0.25^\circ$ , which were further regridded to match the OMI  $\text{NO}_2$  grid. The meteorological variables used in this study include 2 m temperature (T), relative humidity at 1000 hPa (RH), surface solar radiation downwards (SSRD), 10 m wind speed (WS), surface pressure (SP), and boundary layer height (BLH) (Weng et al., 2022).

#### 2.1.4 Anthropogenic emission data

Anthropogenic emission data for 2005–2023 were obtained from the Multi-resolution Emission Inventory for China (MEIC, <http://www.meicmodel.org/>, last access: 14 September 2025) developed by Tsinghua University, covering five sectors: power, industry, residential, transportation, and agriculture (Li et al., 2017). MEIC provides ten major species:  $\text{SO}_2$ ,  $\text{NO}_x$ , carbon monoxide (CO), ammonia ( $\text{NH}_3$ ), carbon dioxide ( $\text{CO}_2$ ), non-methane volatile organic compounds (NMVOCs), fine particulate matter ( $\text{PM}_{2.5}$ ), inhalable particles ( $\text{PM}_{10}$ ), black carbon (BC), and organic carbon (OC) (Zheng et al., 2018; Geng et al., 2024). Following Zhang et al. (2024a) and related work linking emissions to  $\text{O}_3$  variability via machine learning (ML), we selected monthly emissions of  $\text{NO}_x$ , NMVOCs, CO, and  $\text{PM}_{2.5}$  as key predictors for diagnosing OFS. All emission data were resampled to  $0.25^\circ \times 0.25^\circ$  to match the grid of satellite  $\text{NO}_2$  data, ensuring spatial consistency across datasets.

#### 2.1.5 Surface observation data

Surface  $\text{O}_3$  concentration data for 2015–2023 ( $\mu\text{g m}^{-3}$ ) used in this study were obtained from China's national air quality monitoring network. Since 2015, this network has expanded to include more than 330 cities and over 1400 monitoring stations nationwide. The data were collected from the National Real-time Urban Air Quality Publishing Platform provided by the China National Environmental Monitoring Centre (<https://air.cnemc.cn:18007/>, last access: 20 January 2026).

## 2.2 Methodology

### 2.2.1 Diagnosis of OFS and derivation of FNR threshold ranges

OFS was diagnosed using the satellite-based HCHO/ $\text{NO}_2$  ratio (FNR), defined as:

$$\text{FNR} = \frac{[\text{HCHO}]}{[\text{NO}_2]}, \quad (1)$$

where [HCHO] and [ $\text{NO}_2$ ] represent the tropospheric column densities of HCHO and  $\text{NO}_2$ , respectively. Because the two quantities have the same units, FNR is dimensionless.

OFS regimes were then identified according to the corresponding FNR threshold ranges. The threshold ranges were

determined mainly following the method of Jin et al. (2020). In this study, region-specific FNR thresholds across China were derived by combining OMI satellite observations with surface  $\text{O}_3$  measurements. This approach is also consistent with previous studies that derived threshold ranges from fitted  $\text{O}_3$ –FNR relationships (Wang et al., 2021; Ren et al., 2022; Chen et al., 2024). In practice, the transition of OFS from VOC-limited to  $\text{NO}_x$ -limited regimes is gradual rather than abrupt. This transition can be influenced by multiple factors, including topography, meteorological conditions, and the spatial resolution of satellite observations (Jin et al., 2020). Because these influencing factors vary across China, the corresponding FNR threshold ranges are also expected to differ among regions. For this reason, OFS regimes were identified using region-specific FNR threshold ranges. China was divided into six regions, including five major urban clusters with severe  $\text{O}_3$  pollution, namely BTH, FWP, YRD, SCB, and PRD, and one additional category comprising all remaining areas, referred to as other regions of China (ORC) (Lu et al., 2018). These six regions were used as the basic units for deriving region-specific FNR threshold ranges, which were then applied to identify OFS regimes in each region.

Because  $\text{O}_3$  pollution in China occurs mainly during the warm season (April–September) (Lu et al., 2020b), the analysis was restricted to April–September in 2015–2023. To match the OMI overpass time, surface  $\text{O}_3$  concentrations at 13:00 and 14:00 LT were averaged for each site and day. The resulting daily  $\text{O}_3$  concentrations were then collocated with OMI FNR values at the corresponding grid cells. For each site, the high- $\text{O}_3$  probability was then defined as the fraction of days during the study period on which the 13:00–14:00 mean  $\text{O}_3$  concentration exceeded  $160 \mu\text{g m}^{-3}$ . The resulting paired samples were subsequently pooled within each region for threshold derivation.

To focus on polluted conditions, samples with  $\text{NO}_2$  vertical column densities below  $1.5 \times 10^{15}$  molec.  $\text{cm}^{-2}$  were excluded, following previous studies (Jin et al., 2020; Wang et al., 2021). In addition, high-end outliers (5% or 10%, depending on the region) were removed prior to fitting to reduce the influence of extreme values (Chen et al., 2024). After quality control, paired high- $\text{O}_3$  probability and FNR samples in each region were grouped into 100 bins according to FNR and a cubic polynomial was fitted to the binned relationship between high- $\text{O}_3$  probability and FNR. The FNR interval corresponding to fitted high- $\text{O}_3$  probability values above the 90th percentile was then defined as the threshold range for that region (Jin et al., 2020).

### 2.2.2 Trend analysis and statistical testing methods

To quantify the spatiotemporal trends of  $\text{NO}_2$  and HCHO columns during the warm season (April–September) from 2005 to 2023, we applied the nonparametric Mann–Kendall (MK) test for trend significance (Hirsch et al., 1982) and the

Sen's slope for trend magnitude (Sen, 1968). The MK statistics are computed from all pairwise differences in a time series:

$$S = \sum_{i=1}^{n-1} \sum_{j=i+1}^n \text{sgn}(x_j - x_i), \quad (2)$$

where  $n$  is the number of observations,  $x_i$  and  $x_j$  are values at times  $i$  and  $j$ , respectively ( $j > i$ ), and  $\text{sgn}(\cdot)$  is the sign function that quantifies the direction of change between two observations: it returns 1 when a later value ( $x_j$ ) is greater than an earlier one ( $x_i$ ),  $-1$  when it is less, and 0 when they are equal. A positive (negative)  $S$  indicates an increasing (decreasing) trend. Statistical significance is assessed using the standardized test statistic  $Z$ :

$$Z = \begin{cases} \frac{S-1}{\sqrt{\text{Var}(S)}} & S > 0 \\ 0 & S = 0 \\ \frac{S+1}{\sqrt{\text{Var}(S)}} & S < 0 \end{cases}, \quad (3)$$

where  $\text{Var}(S)$  represents the variance of the statistic  $S$ . When  $|Z| \geq 1.96$ , the trend is considered statistically significant at the 95 % confidence level ( $p < 0.05$ ).

Trend magnitude is estimated by the Sen's slope  $\beta$ , defined as the median of all pairwise slopes:

$$\beta = \text{Median} \left( \frac{x_j - x_i}{t_j - t_i} \right), \quad (4)$$

where  $t_i$  and  $t_j$  represent the time points of observations  $i$  and  $j$ , respectively. This MK–Sen framework is distribution-free and robust to outliers, making it well suited to satellite-derived time series.

To further identify structural shifts in the long-term evolution of  $\text{O}_3$  precursors and OFS, and to provide an objective basis for subsequent phase-based analyses, we applied the Pettitt test to the annual time series of  $\text{NO}_2$ , HCHO, and FNR in each region. The Pettitt test is a non-parametric method for detecting a single abrupt change point in a time series and does not require the data to follow a normal distribution (Pettitt, 1979). It has been widely used in environmental studies to detect statistically significant shifts in long-term observations (Baruah et al., 2022). The test statistic  $U_{t,n}$  is defined as:

$$U_{t,n} = \sum_{i=1}^t \sum_{j=t+1}^n \text{sgn}(x_j - x_i) \quad (t = 1, 2, \dots, n), \quad (5)$$

where  $x_i$  and  $x_j$  are the values of the time series, and  $\text{sgn}(\cdot)$  denotes the sign function. The change point is identified as the time corresponding to the maximum absolute value of  $U_{t,n}$ , and its significance is evaluated as:

$$p = 2 \exp \left( -\frac{6k_t^2}{n^3 + n^2} \right), \quad (6)$$

where  $k_t = \max_{1 \leq t < n} |U_{t,n}|$ . A  $p$  value below 0.05 was considered statistically significant.

In this study, the Pettitt test was applied to the annual warm-season (April–September) series of  $\text{NO}_2$ , HCHO, and FNR for each region during 2005–2023. For each variable, the year corresponding to the maximum absolute test statistic was taken as the detected change point. Because the Pettitt test identifies only one abrupt change point, it may not fully capture series with multiple shifts or several equally strong candidates (Zhang and Song, 2015). Therefore, the detected change points were interpreted together with the temporal evolution of each variable and the broader policy context.

### 2.2.3 Machine learning model

Random Forest (RF) is an ensemble machine learning (ML) algorithm based on multiple decision trees and is widely used for classification and regression (Breiman, 2001). It implements Bootstrap aggregation (bagging): each tree is trained on a bootstrap replica of the training data with feature randomness at each split, and predictions are combined by majority vote for classification or arithmetic averaging for regression to improve generalization and robustness (Breiman, 1996).

Departing from most studies that regress  $\text{O}_3$  concentrations on candidate factors (Luo et al., 2024; Yao et al., 2024), we frame the problem as classification to identify the key factors distinguishing OFS regimes. In this setting, the RF seeks to minimize overall misclassification. Given an input and an ensemble of trees, the predicted class is the plurality vote:

$$\hat{y} = \text{argmax}_k \sum_{t=1}^T I(h_t(x) = k), \quad (7)$$

where  $I(\cdot)$  is the indicator function, equal to 1 if the  $t$ th tree assigns the sample to class  $k$ , and 0 otherwise.

This study constructs RF classification models for five city clusters, including BTH, FWP, YRD, SCB, and PRD, to characterize the relationships between OFS, defined based on the FNR classification, and multiple environmental factors. Predictor variables included anthropogenic emissions, namely  $\text{NO}_x$ , NMVOCs, CO, and  $\text{PM}_{2.5}$ , as well as meteorological parameters, including T, RH, SSRD, WS, SP, and BLH. It should be noted that, although OFS is diagnosed here using the FNR indicator, the spatiotemporal distribution of FNR-derived OFS states is jointly shaped by precursor emissions, chemical transformation, transport, dilution, and boundary-layer mixing (Bai et al., 2018; Chen et al., 2020; Liu and Shi, 2021). Meteorological conditions therefore do not enter the OFS definition directly but can influence the probability of different OFS states by modulating the underlying precursor environment. Based on this rationale, we treat the diagnosed OFS regimes as response classes and use RF to statistically map their relationships with meteorological and emission-related predictors.

Model training and evaluation were based on annual mean gridded data for the warm seasons (April–September) from 2005 to 2023. Because the primary aim of this study was not

to predict OFS in future years, but to characterize the relationships between OFS regimes and their environmental factors over the full study period, a year-wise stratified random sampling strategy was adopted. In studies aimed at predicting future years, a common practice is to train the model on earlier-period data and validate it on later-period data in order to assess temporal extrapolation skill (Ni et al., 2024; Wang et al., 2023). Such a strategy was not adopted here because it would bias model evaluation and subsequent SHAP interpretation toward the late-period data distribution. Instead, samples from each year were randomly divided into 80 % for training and 20 % for validation (Özüpak et al., 2025), so that both subsets contained data from all years. This design preserves interannual variability associated with key periods, including major policy interventions and the COVID-19 pandemic, while maintaining comparable sample distributions across the training and validation sets. In addition, given the class imbalance in the dataset, this stratified sampling strategy helps maintain a more balanced class distribution in both subsets, thereby improving the reliability of model evaluation (Sadaiyandi et al., 2023). It also provides a more suitable basis for subsequent SHAP-based interpretation across different temporal subsets, thereby facilitating comparisons of OFS regimes before and after policy implementation.

To account for class imbalance and optimize model performance, the Synthetic Minority Over-sampling Technique (SMOTE; Fernandez et al., 2018) was applied to the training data. To reduce the structural differences of the model and facilitate consistent comparison across the five regions, a unified set of model parameters was adopted for all regional models. Although this does not eliminate differences in model baseline and data distribution across regions, it helps ensure that the regional models are constructed under a consistent modeling framework. Hyperparameter optimization was performed using GridSearchCV (Hastie et al., 2009; Ahmed et al., 2025) over combinations of candidate parameter values. Based on validation performance across all regions, a single parameter set was selected as the optimal configuration. The final model configuration consisted of 200 trees ( $n_{\text{estimators}}=200$ ), a maximum tree depth of 25 ( $\text{max\_depth}=25$ ), and a minimum of 1 sample per leaf ( $\text{min\_samples\_leaf}=1$ ).

Model performance on the validation set was evaluated using multiple metrics, including precision score (PS), recall score (RS), F1-score (F1), accuracy score (AS), geometric mean score (GMS), and the Area Under the Curve of the Receiver Operating Characteristic (ROC-AUC) score (Thieu, 2024; Ahmed et al., 2025). All of these metrics range from 0 to 1, with higher values indicating better performance.

#### 2.2.4 SHapley Additive exPlanations approach

SHapley Additive exPlanations (SHAP) is an interpretable ML framework based on cooperative game theory that explains model prediction by assigning each feature a Shapley

value representing its contribution to the prediction (Lundberg and Lee, 2017). It is defined as follows:

$$\varphi_i = \sum_{S \subseteq \{1, \dots, n\} \setminus \{i\}} \frac{|S|!(n - |S| - 1)!}{n!} [f(S \cup \{i\}) - f(S)], \quad (8)$$

where  $\varphi_i$  is the SHAP value of feature  $i$ ,  $S$  represents the feature subset excluding feature  $i$ ,  $f(S \cup \{i\})$  and  $f(S)$  are the model predictions for the corresponding subsets, and  $\frac{|S|!(n - |S| - 1)!}{n!}$  ensures that the contributions of all feature subsets are fairly distributed.

A positive SHAP value indicates that a given feature increases the model prediction, whereas a negative SHAP value indicates that it decreases the prediction. In this study, SHAP values were calculated for the RF models in different regions to identify the key factors of OFS regimes, including  $\text{NO}_x$ -limited, transitional, and VOC-limited regimes, and to further interpret the direction and relative magnitude of their effects.

For each regional model, the mean absolute SHAP value [ $\text{mean}(|\text{SHAP}|)$ ] was calculated for each feature. Because SHAP values are defined relative to the model-specific expected output and are influenced by the underlying data distribution, the absolute magnitudes of SHAP values are not directly comparable across different regional models. Therefore, to facilitate cross-region comparison, these overall  $\text{mean}(|\text{SHAP}|)$  values were further normalized to obtain the relative contribution of each variable within each regional model. It should be noted that this metric reflects the statistical contribution of individual features to model predictions rather than their direct causal effects in atmospheric physical or chemical processes.

### 3 Results and discussion

#### 3.1 Spatiotemporal evolution of ozone precursors

Before examining the spatial and temporal evolution of  $\text{O}_3$  precursors and FNR, we first assessed whether their long-term changes were characterized by structural shifts. Pettitt test results (Table S2 in the Supplement) indicate that significant change points in warm-season  $\text{NO}_2$ , HCHO, and FNR were generally clustered around 2013–2017, although the exact timing varied among variables and regions. Because these shifts broadly coincided with the implementation of the Air Pollution Prevention and Control Action Plan (2013–2017), 2013 was adopted as the common dividing year for the subsequent analyses. The following sections therefore compare the two periods 2005–2012 and 2013–2023.

Under this phase-based framework, the spatial patterns and long-term trends of tropospheric  $\text{NO}_2$  and HCHO columns were further examined (Fig. 2). High  $\text{NO}_2$  columns are mainly concentrated in densely populated and industrialized urban clusters, including the BTH, YRD, and PRD

regions (Fig. 2a), reflecting intensive energy use and traffic emissions in eastern China (Fu et al., 2022). Among the five key regions, BTH shows the highest annual mean  $\text{NO}_2$  column ( $7.41 \times 10^{15}$  molec.  $\text{cm}^{-2}$ ), which is 2.56 times that in SCB ( $2.90 \times 10^{15}$  molec.  $\text{cm}^{-2}$ ) (Fig. S1 in the Supplement). This pattern is consistent with the concentration of heavy industry (e.g., steel production) and the widespread use of coal for winter heating in northern China (Li et al., 2010; Feng et al., 2014). In terms of temporal evolution,  $\text{NO}_2$  showed a clear phase shift around 2013. From 2005 to 2012,  $\text{NO}_2$  increased by 31.5 % at the national scale, with the strongest growth occurring in eastern China and a maximum trend of  $1.16 \times 10^{15}$  molec.  $\text{cm}^{-2} \text{yr}^{-1}$ . The PRD was a notable exception in which  $\text{NO}_2$  decreased by 23.3 % during the same period, with a maximum trend of  $-1.21 \times 10^{15}$  molec.  $\text{cm}^{-2} \text{yr}^{-1}$ , likely reflecting earlier industrial restructuring and vehicle emission controls (Bian et al., 2019; Lu et al., 2020a). After the implementation of major clean air policies in 2013,  $\text{NO}_2$  showed a widespread decline across China (Fig. 2c), with a national decrease of 27.6 % and the largest reductions occurring in eastern urban clusters. The maximum decline reached  $-1.37 \times 10^{15}$  molec.  $\text{cm}^{-2} \text{yr}^{-1}$ , indicating a clear response of  $\text{NO}_x$  to emission-control policies (Shah et al., 2020; Li et al., 2023). This shift in  $\text{NO}_2$  is an important background for subsequent changes in OFS.

Compared with  $\text{NO}_2$ , HCHO exhibits a more complex spatial distribution. Elevated HCHO columns are observed not only over the major urban clusters in eastern China, but also across parts of southwestern and western China, including Guangxi, Yunnan, western Sichuan, and southern Tibet, where the values can even exceed those over some eastern urban regions (Fig. 2d). Such high values may partly reflect enhanced HCHO production associated with strong biogenic VOCs (BVOCs) emissions under warm conditions and intense solar radiation (Zhang et al., 2025a). However, they may also be influenced by the relatively large retrieval uncertainties in western China, especially over the Qinghai–Tibet Plateau and surrounding areas, where complex terrain and surface conditions can affect satellite retrieval accuracy (Fig. S2; Xia et al., 2024). Therefore, the elevated HCHO columns in these regions likely result from a combination of real atmospheric signals and retrieval uncertainties and should be interpreted with caution. Among the five key regions, the PRD has the highest annual mean HCHO column ( $10.60 \times 10^{15}$  molec.  $\text{cm}^{-2}$ ) (Fig. S1), reflecting the combined influence of strong anthropogenic emissions and substantial biogenic contributions (Xia et al., 2024).

The temporal evolution of HCHO differs markedly from that of  $\text{NO}_2$ . During 2005–2012, HCHO increased modestly at the national scale, with an average trend of  $0.17 \times 10^{15}$  molec.  $\text{cm}^{-2} \text{yr}^{-1}$ , corresponding to an increase of 19.5 %. The most pronounced increases occurred along the urban corridor from North China to East China. From 2013 to 2023, a clear increasing trend emerged over large

parts of northwestern China, and the national HCHO column increased by 20.8 %. The continued rise after 2013 may be related to two factors. First, regional warming and enhanced shortwave radiation can stimulate BVOCs emissions (Wang et al., 2024). Second,  $\text{NO}_x$  emissions declined more rapidly than anthropogenic VOCs (AVOCs) (Itahashi et al., 2022), which may have altered the photochemical environment and increased both the production efficiency and atmospheric lifetime of HCHO. The sustained increase in HCHO is also consistent with the continued rise in surface  $\text{O}_3$  observed in China over the past decade (Wang et al., 2022).

Overall, the long-term evolution of  $\text{O}_3$  precursors reflects the combined influence of emission-control policies and climate-related factors.  $\text{NO}_x$  declined substantially in response to anthropogenic emission reductions, whereas HCHO continued to increase in many regions, consistent with previous studies (Bauwens et al., 2022), and these HCHO changes have been primarily attributed to meteorological variability and natural emissions (Itahashi et al., 2022; Vazquez Santiago et al., 2024). This asynchronous evolution of  $\text{NO}_2$  and HCHO provides an important precursor basis for the subsequent shifts in FNR and OFS across China.

### 3.2 Determination of region-specific FNR threshold ranges

To derive region-specific FNR threshold ranges, we first examined the nonlinear relationship between  $\text{O}_3$  formation and its precursors using satellite-derived HCHO and  $\text{NO}_2$ . Figure S3 shows the distribution of high- $\text{O}_3$  probability in the two-dimensional HCHO– $\text{NO}_2$  space for the six regions. The overall pattern is similar to the  $\text{O}_3$  contour structure reported in previous studies (Sillman, 1999), indicating that HCHO and  $\text{NO}_2$  can reasonably serve as proxies for VOCs and  $\text{NO}_x$ , respectively, in characterizing the nonlinear response of  $\text{O}_3$  formation. Based on this relationship, each region can be broadly divided into three OFS regimes: a  $\text{NO}_x$ -limited regime under relatively high HCHO and low  $\text{NO}_2$  conditions, a transitional regime under relatively high levels of both HCHO and  $\text{NO}_2$ , and a VOC-limited regime under relatively low HCHO and high  $\text{NO}_2$  conditions.

Based on the fitted high- $\text{O}_3$  probability–FNR relationships, region-specific threshold ranges were derived for the six regions, reflecting the gradual transition among OFS regimes. Figure 3 shows the fitted relationships for the six regions during the warm season (April–September) of 2015–2023. Clear regional differences are found in the derived FNR threshold ranges. Among the six regions, FWP shows the highest threshold range, with a central threshold of 3.42 and a range of [2.26, 4.77], whereas YRD shows the lowest, with a central threshold of 1.59 and a range of [0.90, 2.37]. The corresponding threshold ranges for BTH, SCB, PRD, and ORC are [1.51, 3.30], [1.93, 4.73], [1.66, 3.70], and [1.17, 3.08], respectively. In terms of fitting performance, the correlation

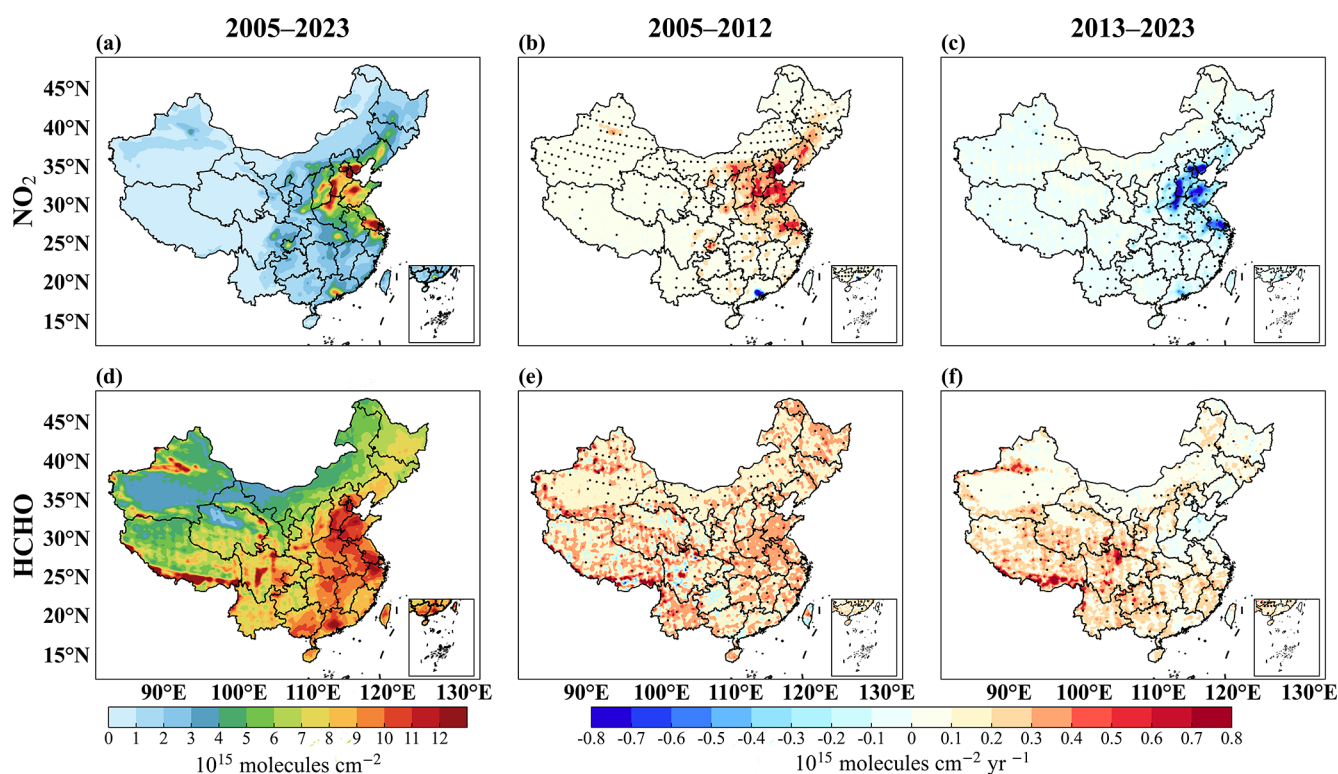


**Figure 2.** Spatiotemporal variations of tropospheric  $\text{NO}_2$  and  $\text{HCHO}$  columns over China during the warm season (April–September) from 2005 to 2023. (a, d) Distribution of annual average columns for 2005–2023; spatial distributions of the Sen's slope and Mann–Kendall (MK) test results for annual means during (b, e) 2005–2012 and (c, f) 2013–2023. Black dots in panels (b), (c), (e), (f) mark grids that pass the MK significance test ( $p < 0.05$ ).

coefficient is 0.58 in FWP and exceeds 0.60 in the other regions, reaching 0.96 in ORC, with all  $p$  values below 0.05. These results indicated that the fitted curves generally capture the variation in high- $\text{O}_3$  probability well. Comparison with previous studies (Table S1) further shows that FNR thresholds vary across regions, reflecting differences in atmospheric environment, precursor emissions, and local conditions (Liu and Shi, 2021).

Given these pronounced regional differences, we further assessed how threshold uncertainty affects OFS classification. Three threshold-range scenarios were designed. Specifically, Scenario 1 (S1) used the threshold ranges derived in this study for the warm season of 2015–2023, Scenario 2 (S2) adopted the minimum–maximum threshold ranges reported in previous studies, and Scenario 3 (S3) used threshold ranges calculated from the average of the corresponding maximum and minimum values. The threshold ranges for the six regions under S1–S3 scenarios are listed in Table S1. These three scenarios were then used to evaluate the sensitivity of OFS classification to different FNR threshold selections in the five major city clusters during the warm season over 2005–2023 (Fig. S4).

The results show that OFS classification is strongly affected by threshold choice, although the magnitude of this ef-

fect varies markedly across regions. Among the five regions, FWP shows the largest sensitivity to threshold variation, with changes ranging from  $-53.8\%$  to  $51.6\%$  and an average value of about  $22.0\%$ . SCB also exhibits substantial sensitivity, with corresponding changes of  $-48.8\%$  to  $52.0\%$ . In contrast, PRD is relatively less sensitive, with changes ranging from  $-36.3\%$  to  $21.1\%$  and an average value of about  $17.0\%$ . BTH and YRD show intermediate responses, with ranges of  $-31.0\%$  to  $37.2\%$  and  $-31.5\%$  to  $31.5\%$ , respectively. These results indicate that the uncertainty introduced by threshold selection is not spatially uniform but depends on regional photochemical characteristics and the width of the transitional range.

Figure S4 further shows that the influence of threshold choice is often asymmetric, with some scenarios producing much larger positive or negative deviations than others. This indicates that OFS classification does not respond linearly to threshold perturbations. In particular, threshold ranges compiled from previous studies can produce substantial departures from the classification results obtained using the region-specific thresholds derived here. Even the average-threshold scenario still leads to noticeable deviations in several regions. These findings suggest that threshold transferability across regions is limited and that applying literature-based thresh-

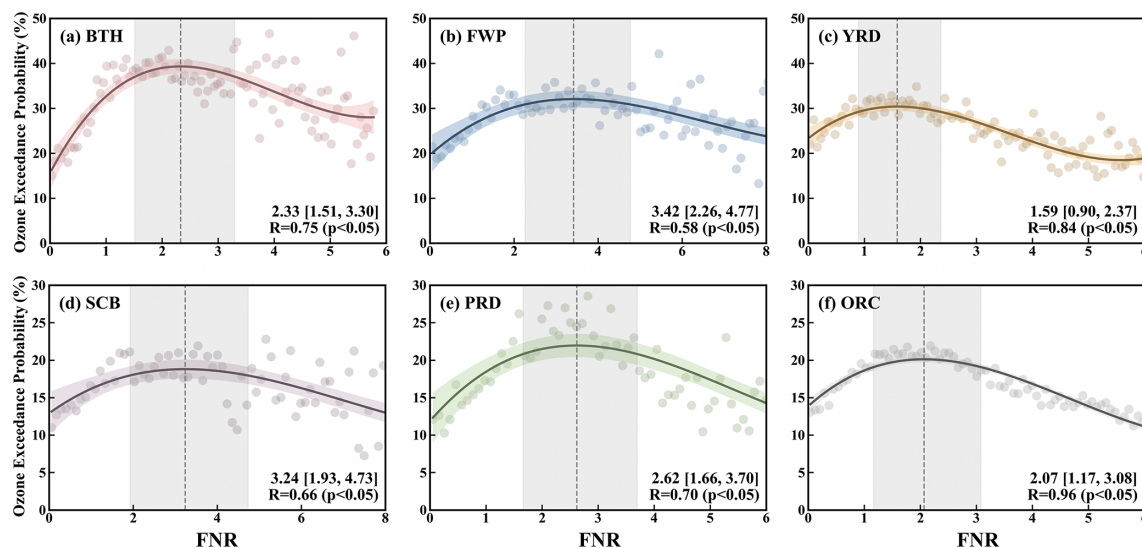


**Figure 3.** Relationship between daily high- $O_3$  probability and FNR in the six regions during the warm season (April–September) of 2015–2023. Solid lines show the fitted cubic polynomial curves, and the shaded areas indicate the 95 % confidence intervals. Vertical dashed lines mark the peak values of the fitted curves, while the gray shaded bands denote the FNR ranges corresponding to the upper 10 % of the fitted curves, which were used to define the threshold ranges.

olds without regional constraints may introduce considerable bias into OFS diagnosis.

Overall, these results demonstrate that uncertainty in FNR thresholds can substantially alter the estimated proportions of different OFS regimes. Region-specific thresholds derived from regional observational relationships therefore provide a more robust basis for OFS classification than fixed or literature-averaged thresholds.

### 3.3 Spatiotemporal evolution of ozone formation sensitivity regimes

#### 3.3.1 Interannual variations of regional FNR

The derived region-specific FNR thresholds were used to diagnose OFS during the warm season (April–September) from 2005 to 2023. Overall, BTH, FWP, and YRD show a clear two-stage evolution in FNR (Fig. 4). From 2005 to 2012, FNR remained relatively stable, with only small interannual variations, because both  $NO_2$  and HCHO increased during this period and their changes largely offset each other in the ratio. In contrast, FNR increased markedly during 2013–2014. This change was mainly driven by a sharp decline in  $NO_2$  together with a continued rise in HCHO, which led to a pronounced increase in FNR and a gradual shift of OFS toward  $NO_x$ -limited regimes. Based on the derived thresholds, BTH and FWP were dominated by VOC-limited and transitional regimes during the warm season, whereas YRD was characterized primarily by transitional and  $NO_x$ -limited regimes. This evolution likely reflects the combined influence of emission-control policies and climate-related factors. On the one hand, major clean-air policies imple-

mented after 2013 substantially reduced  $NO_x$  emissions. On the other hand, warmer conditions and stronger solar radiation may have enhanced  $O_3$  production efficiency and prolonged the persistence of HCHO (Wu et al., 2024), thereby contributing to higher FNR values and stronger  $NO_x$ -limited characteristics.

In contrast, SCB shows a relatively high annual mean FNR of 3.34 but no significant change point or clear long-term trend. In addition, SCB did not show a statistically significant change point in the Pettitt test, which further supports the decision not to interpret its FNR evolution using the same two-stage framework. Together with the relatively small changes in both  $NO_2$  and HCHO, this suggests that the precursor structure in SCB remained comparatively stable over the study period, and OFS stayed largely within the transitional regime.

PRD differs from the other two patterns by exhibiting a significant long-term increase in FNR, at a rate of  $0.06 \text{ yr}^{-1}$  ( $p < 0.05$ ). This trend indicates a shift in OFS from VOC-limited or transitional regimes toward more  $NO_x$ -limited regimes, likely associated with reductions in  $NO_x$ -rich sources in the region, particularly from road traffic and industrial emissions, as suggested by previous studies (Bian et al., 2019; Li et al., 2025).

The timing of the detected change points broadly coincides with the implementation of major clean-air policies in China, suggesting that precursor control patterns in the major urban clusters changed substantially after the early 2010s. At the same time, under conditions of climate warming and enhanced radiation, and against the background of anthropogenic precursor reductions, continued increases in HCHO

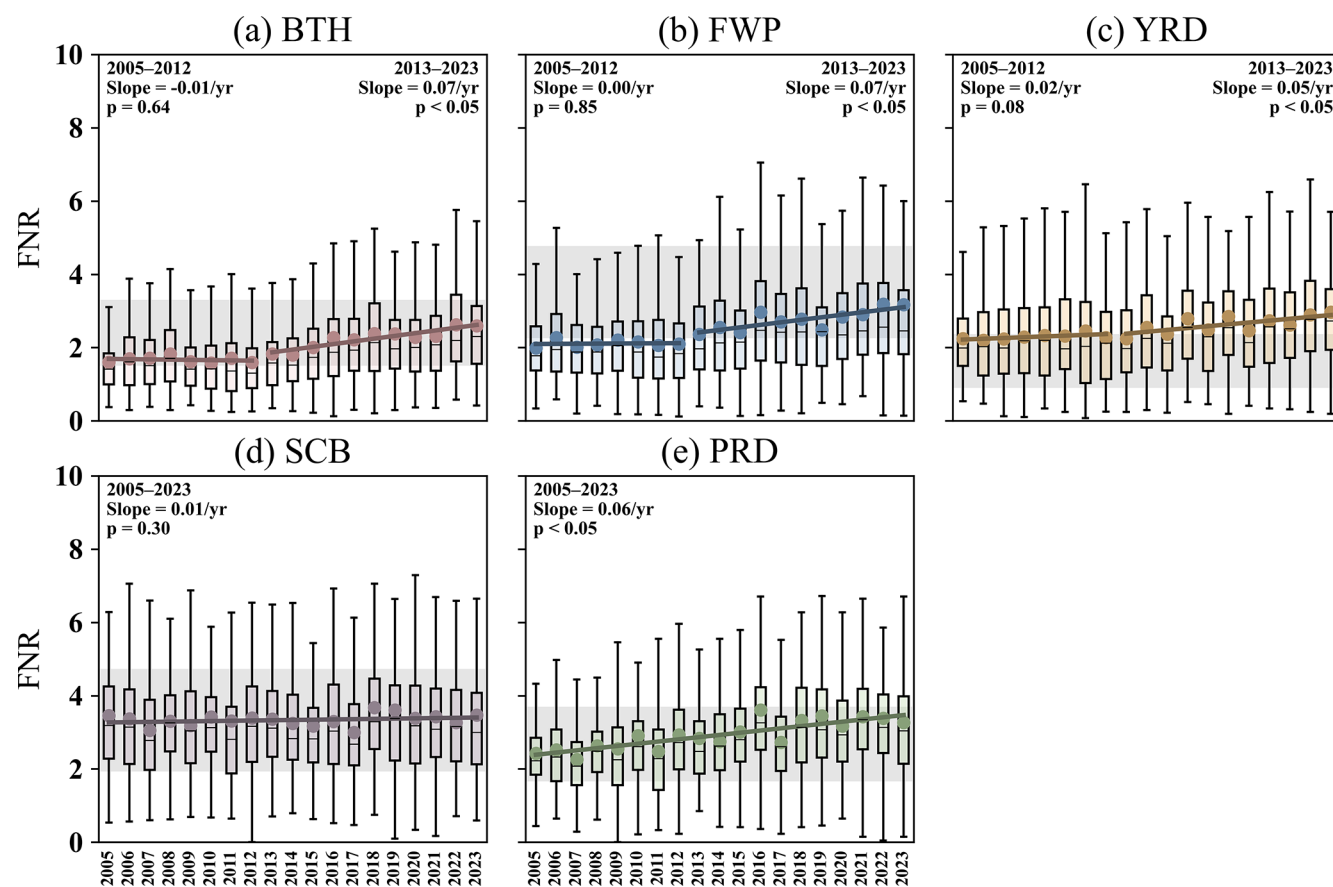


**Figure 4.** Interannual variations in FNR in the key regions during the warm season (April–September) from 2005 to 2023. Box plots show the median (horizontal line), the 25th and 75th percentiles (box boundaries), the minimum and maximum values (whiskers), and the mean (plus signs). The shaded areas indicate the corresponding OFS threshold ranges.

may have further promoted the shift toward more  $\text{NO}_x$ -limited chemistry (Itahashi et al., 2022; Wu et al., 2020).

### 3.3.2 Spatial distribution patterns of ozone formation sensitivity regimes

Based on the OMI-derived FNR, OFS in China during the warm season from 2005 to 2023 shows a clear spatial pattern (Fig. 5). VOC-limited regimes are concentrated mainly in eastern urban clusters, whereas  $\text{NO}_x$ -limited regimes are more common in surrounding suburban and less developed areas. In regions such as BTH and FWP, strong anthropogenic  $\text{NO}_x$  emissions lead to relatively low FNR values, resulting in predominantly VOC-limited regimes in most years. Away from urban cores,  $\text{NO}_x$  emissions gradually decrease, while the relative contribution of BVOCs becomes more important, leading to higher FNR values and a shift toward  $\text{NO}_x$ -limited regimes (Zhang et al., 2017; Wu et al., 2020). This spatial pattern is generally consistent with previous studies and reflects regional differences in emission structure, land cover, and urbanization level (Chen et al., 2020; Ren et al., 2022).

The areal fractions of different OFS regimes also show a clear temporal shift before and after the implementation of the Air Pollution Prevention and Control Action Plan (Fig. 5d). During 2005–2012, the OFS distribution in eastern China shifted toward more VOC-limited regimes, mainly through transitions from  $\text{NO}_x$ -limited to transitional regimes and from transitional to VOC-limited regimes. Over this period, the area fraction of  $\text{NO}_x$ -limited regimes decreased by 7.9%, while the fractions of transitional and VOC-limited regimes increased by 5.6% and 2.3%, respectively. This change is consistent with the faster increase in  $\text{NO}_2$  than in HCHO during this period, which lowered FNR and favored VOC limitation. PRD showed a different evolution, with a decline in VOC-limited regimes and a predominance of transitional regimes by 2012.

During 2013–2023, the national OFS pattern shifted back toward  $\text{NO}_x$ -limited and transitional regimes. This change was associated with substantial reductions in  $\text{NO}_x$  emissions, comparatively slower decreases in anthropogenic VOC emissions (Fig. S5), and continued enhancement of BVOCs emissions under warmer and more strongly irradiated conditions (Zeng et al., 2023; Zhang et al., 2025a). By 2023, VOC-

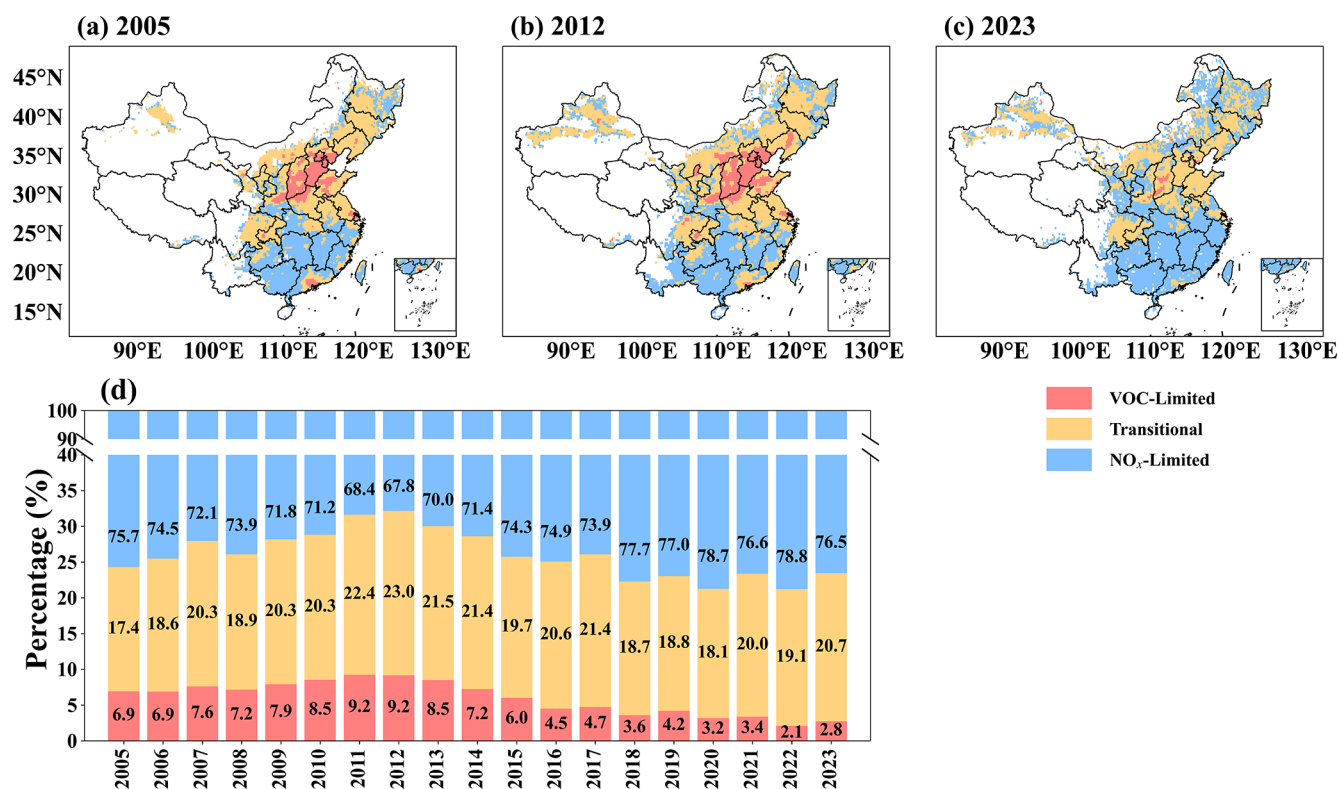


**Figure 5.** Spatial distribution of FNR over China during the warm season (April–September) in (a) 2005, (b) 2012, and (c) 2023; (d) inter-annual variation in the area fractions of different OFS regimes from 2005 to 2023. FNR is shown only for polluted regions, defined as areas with mean OMI NO<sub>2</sub> columns greater than  $1.5 \times 10^{15}$  molec. cm<sup>-2</sup>.

limited regimes accounted for only 2.8 % of the total area, whereas NO<sub>x</sub>-limited regimes expanded to 76.5 %. This evolution indicates that OFS in China did not change monotonically over time but instead underwent a pronounced reversal under the combined influence of emission-control policies and climate-related factors (Fang et al., 2026). It also highlights the asymmetric reduction of O<sub>3</sub> precursors during China's clean-air actions and the resulting shifts in regional O<sub>3</sub> chemistry.

### 3.3.3 Impact of short-term COVID-19 lockdown on ozone formation sensitivity regimes

The nationwide COVID-19 lockdown in early 2020 caused a sharp but short-lived reduction in anthropogenic emissions and provided a useful case for examining the response of OFS to abrupt emission changes. To capture this process, the period was divided into three phases: pre-lockdown (1–22 January 2020; 22 d), during lockdown (23 January–13 February 2020; 22 d), and post-lockdown (14 February–7 March 2020; 23 d).

Figure 6 shows the spatial distributions of O<sub>3</sub> precursors and FNR during these three phases. Before the lockdown, high tropospheric NO<sub>2</sub> columns formed a continuous belt across the urban-industrial regions of North, East, and South

China. During the lockdown, both the intensity and spatial extent of high NO<sub>2</sub> decreased markedly, consistent with strong reductions in industrial activity and traffic emissions. In the post-lockdown phase, NO<sub>2</sub> columns recovered partially in many regions, although they remained below pre-lockdown levels (Qiao et al., 2022; Zhao et al., 2022). HCHO showed a broadly similar pattern, but its spatial changes were less uniform. During the post-lockdown phase, HCHO increased over parts of South and Southwest China. This increase was likely related to the combined influence of wildfire emissions from Myanmar and northern Vietnam and enhanced BVOCs emissions (Stavrakou et al., 2021). These results suggest that seasonal and BVOCs sources played an important role in sustaining HCHO levels and increasing FNR during this period.

The corresponding OFS distributions also changed substantially across the three phases. Before the lockdown, VOC-limited and transitional regimes dominated most major urban regions in eastern China. During the lockdown, the sharp decline in NO<sub>2</sub> led to a rapid increase in FNR and a broad expansion of NO<sub>x</sub>-limited regimes. This shift was especially evident in PRD and YRD, where OFS changed rapidly from VOC-limited toward transitional or NO<sub>x</sub>-limited regimes. Such changes are consistent with strong NO<sub>x</sub> reductions that weakened urban O<sub>3</sub> titration and al-

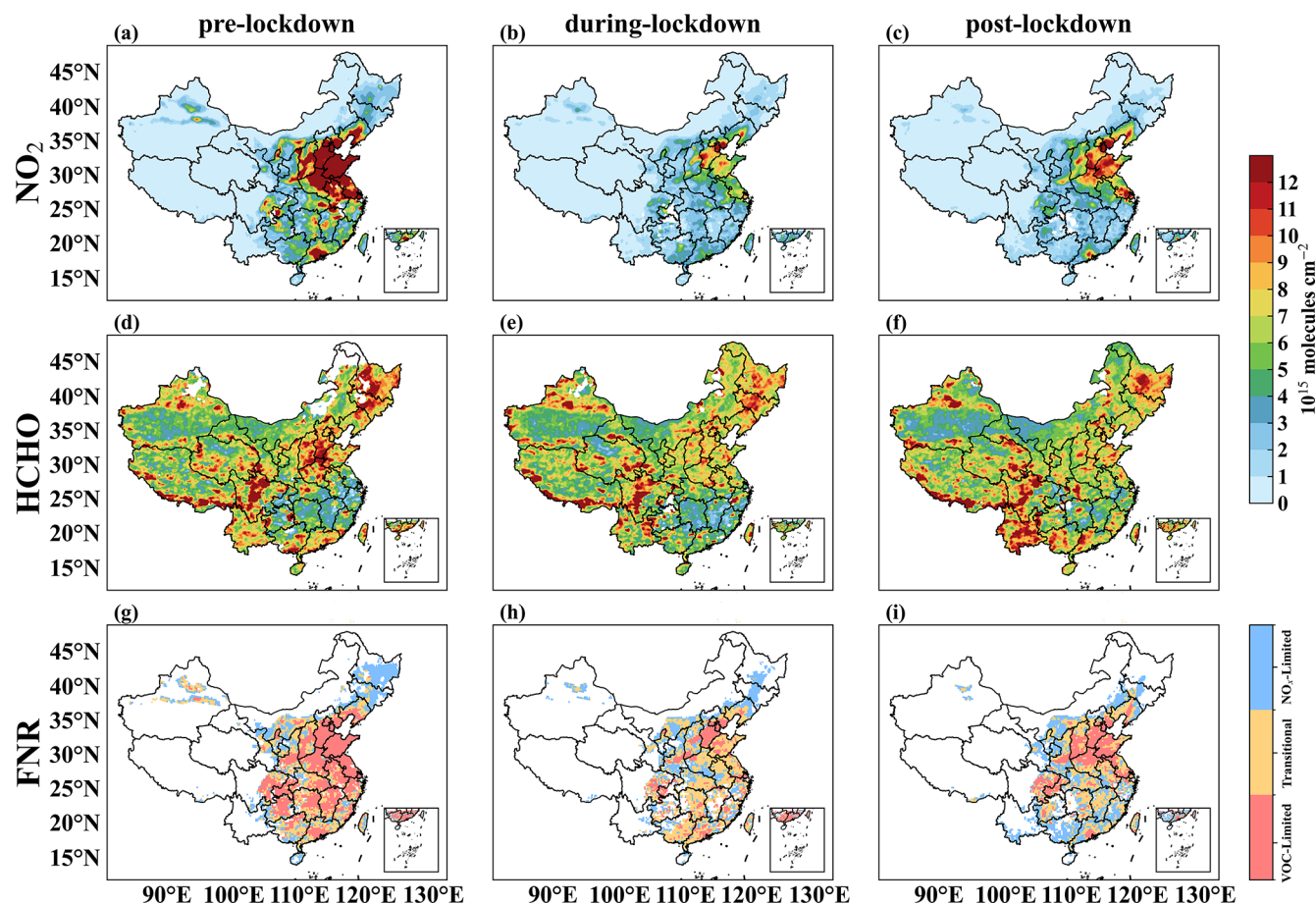


**Figure 6.** Spatial patterns of tropospheric  $\text{NO}_2$  and HCHO columns, and FNR during the pre-, during-, and post-lockdown phases of early 2020. FNR is shown only for polluted regions, defined as areas with mean OMI  $\text{NO}_2$  columns greater than  $1.5 \times 10^{15}$  molec.  $\text{cm}^{-2}$ .

tered precursor limitation. In the post-lockdown phase, as  $\text{NO}_x$  emissions partly recovered, parts of the North China Plain and northern YRD shifted back toward VOC-limited and transitional regimes. However, the spatial extent of these regimes did not return to pre-lockdown levels.

The short-term OFS response during the COVID-19 lockdown is broadly consistent with the longer-term evolution observed from 2005 to 2023. In both cases, rapid reductions in  $\text{NO}_x$  promoted a shift toward more  $\text{NO}_x$ -limited regimes, whereas partial  $\text{NO}_x$  recovery or enhanced VOC emissions tended to move OFS back toward transitional or VOC-limited regimes. These results indicate that OFS in China is highly sensitive to short-term emission perturbations, especially under meteorological conditions favorable for photochemical production. They also suggest that the effectiveness of  $\text{O}_3$  control depends strongly on precursor reduction pathways and background climatic conditions. In warm-season urban regions, sustained  $\text{NO}_x$  reductions are more likely to support  $\text{O}_3$  mitigation, whereas coordinated VOC control remains important in regions or periods where OFS may shift back toward transitional or VOC-limited regimes.

### 3.4 Attribution of factors influencing OFS via explainable machine learning

#### 3.4.1 Performance of RF models for OFS classification

Table 1 presents a comparison of the five model configurations. Overall, all models demonstrate relatively high classification performance, with AS, GMS, and ROC-AUC all exceeding 0.70. Among the regions, the models for the YRD and PRD perform the best, with all category-specific metrics generally above 0.70.

In contrast, the BTH and FWP models show relatively low performance for minority classes, particularly the  $\text{NO}_x$ -limited category, with F1 scores of 0.60 and 0.57, respectively, while other categories generally achieve metrics above 0.60, indicating moderate performance in identifying this category. In the SCB model, the  $\text{NO}_x$ -limited category performs the worst, with PS, RS, and F1 all below 0.50, reflecting the difficulty for the model in effectively capturing its characteristics.

Overall, after sampling and hyperparameter optimization, the models achieve robust performance on the majority

**Table 1.** Performance metrics of the optimized model on the validation dataset.

Models	Class	PS	RS	F1	AS	GMS	ROC-AUC
BTH	NO <sub>x</sub> -limited*	0.51	0.73	0.60	0.94	0.83	0.96
	VOC-limited	0.88	0.88	0.90	0.88	0.89	0.95
	Transitional	0.83	0.78	0.81	0.83	0.82	0.90
FWP	NO <sub>x</sub> -limited*	0.51	0.64	0.57	0.96	0.79	0.97
	VOC-limited	0.88	0.88	0.88	0.86	0.85	0.93
	Transitional	0.75	0.72	0.74	0.82	0.79	0.89
YRD	NO <sub>x</sub> -limited	0.84	0.87	0.85	0.89	0.88	0.95
	VOC-limited*	0.69	0.75	0.72	0.98	0.86	0.99
	Transitional	0.90	0.87	0.88	0.87	0.86	0.93
SCB	NO <sub>x</sub> -limited*	0.32	0.48	0.39	0.90	0.67	0.87
	VOC-limited*	0.51	0.68	0.58	0.94	0.81	0.92
	Transitional	0.94	0.89	0.91	0.85	0.72	0.81
PRD	NO <sub>x</sub> -limited	0.85	0.82	0.84	0.92	0.88	0.96
	VOC-limited*	0.66	0.80	0.72	0.90	0.86	0.94
	Transitional	0.86	0.82	0.84	0.81	0.81	0.88

\* Minority classes (categories with fewer samples).

classes, but classification performance for minority classes remains limited. Ahmed et al. (2025) noted that SMOTE can effectively improve classification performance by addressing data imbalance, but it may also lead to decreased accuracy for majority classes, highlighting the trade-offs involved when handling imbalanced datasets.

### 3.4.2 Relative contributions and regional heterogeneity of OFS influencing factors

For each regional model, SHAP values were first calculated for each sample and for each OFS class. For each class, mean(|SHAP|) was then computed for each feature across all samples, and these class-specific mean(|SHAP|) values were subsequently averaged across the three OFS classes to represent the overall importance of each feature in that regional model. To facilitate comparison among regions, the resulting overall mean(|SHAP|) values were further normalized and expressed as relative contribution percentages. Figure 7 shows the relative contribution of each feature to OFS classification in the five city clusters. Overall, emission-related variables contribute more than meteorological variables, with their total contribution ranging from 50.1 % in YRD to 72.2 % in PRD. This result indicates that OFS classification is primarily constrained by emission-related factors in most city clusters. In YRD, meteorological and emission-related variables contribute almost equally to OFS classification, accounting for 49.9 % and 50.1 %, respectively.

A closer examination of individual emission predictors reveals substantial regional heterogeneity. In BTH, FWP, and YRD, CO and PM<sub>2.5</sub> make the largest contributions (17.5 % and 14.0 % in BTH; 16.3 % and 16.5 % in FWP; 14.3 %

and 13.3 % in YRD). NMVOCs also show a relatively large contribution in BTH, reaching 13.0 %. By contrast, SCB and PRD are characterized by high contributions from CO and NO<sub>x</sub> (19.0 % and 15.9 % in SCB; 24.4 % and 17.6 % in PRD). The strong model importance of CO and PM<sub>2.5</sub> likely reflects both the influence of their significant long-term trends in the model and their broader association with regional photochemical environments. First, both variables show a two-stage trend in most urban clusters from 2005 to 2023, with an initial period of non-significant change followed by a significant decline (Fig. S5), a pattern that is similar to the phase-like changes in OFS identified in this study (Fig. S6). Second, CO can enhance hydroperoxy radical (HO<sub>2</sub>) production through the reaction  $\text{CO} + \text{OH} \rightarrow \text{HO}_2$ , thereby increasing O<sub>3</sub> production efficiency under conditions of declining NO<sub>x</sub> (Ren et al., 2013; Seinfeld and Pandis, 2016). Third, a reduction in PM<sub>2.5</sub> may weaken its heterogeneous uptake of hydroxyl radicals (HO<sub>x</sub>) and NO<sub>x</sub> and thus allow more radicals and reactive nitrogen to remain available for photochemical O<sub>3</sub> reactions (Li et al., 2019). Therefore, these results suggest that CO and PM<sub>2.5</sub> function not simply as co-emitted pollutants, but also as informative predictors of broader changes in oxidation capacity and regional pollution conditions.

Meteorological predictors also show robust and regionally distinct contributions. Surface pressure (SP), relative humidity (RH), and temperature (T) are consistently important across regions, highlighting the roles of weather system stability, moisture conditions and thermal conditions in modulating photochemistry and pollutant accumulation. In the YRD, the contribution of RH is particularly notable (25.5 %), while in the FWP, SP contributes more substan-

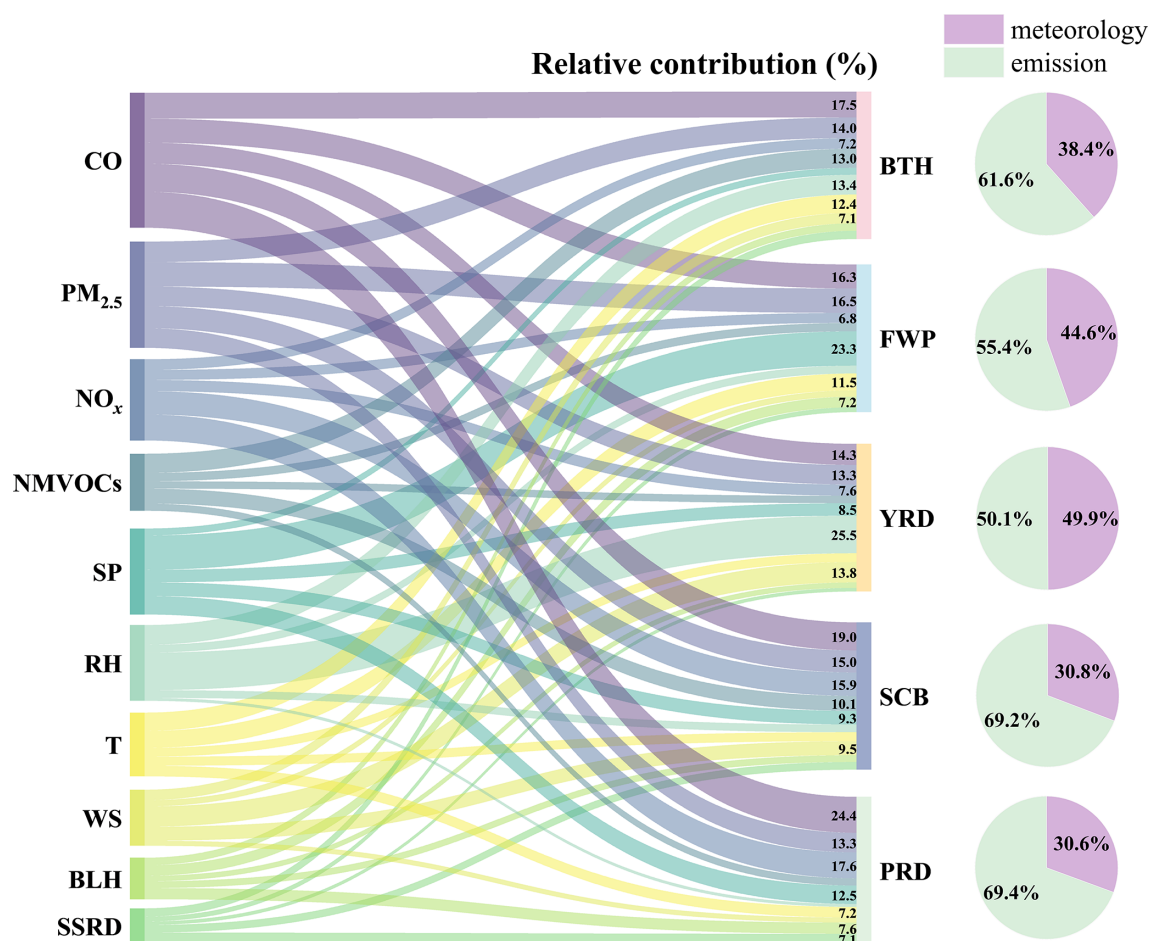


**Figure 7.** Relative contribution of emission-related and meteorological factors to overall OFS classification.

tially (23.3%), indicating that OFS in these regions is also strongly influenced by meteorological factors. More broadly, meteorological factors can influence atmospheric oxidation capacity, boundary-layer structure, and pollutant dispersion, thereby shaping both the spatial distribution and temporal evolution of OFS. Therefore, the relatively high contributions of certain meteorological factors in the YRD and FWP may reflect a greater sensitivity of OFS classification to regional humidity and atmospheric stability conditions.

### 3.4.3 Regional and temporal shifts in OFS-related factor contributions

To further characterize the temporal evolution of the factors influencing OFS, we compared the relative contributions of emission-related and meteorological variables between the warm-season periods of 2005–2012 and 2013–2023 (Fig. 8). Overall, emission-related variables remained the dominant predictors across most urban clusters and OFS categories in both periods, with their contributions generally exceeding 50%. This suggests that the long-term evolution of OFS in China was primarily governed by changes in precursor emis-

sions, although the relative role of meteorology varied by region and OFS category.

For the NO<sub>x</sub>-limited regime, the contributions of meteorological and emission-related factors in YRD were broadly comparable, whereas emission-related contributions in BTH, YRD, and PRD increased slightly after 2013 (+4.6%, +2.2%, and +3.5%, respectively). By contrast, meteorological contributions increased moderately in FWP and SCB (+4.2% and +4.3%, respectively). In the VOC-limited and transitional regimes, emission-related factors also remained dominant overall. However, meteorological contributions to the VOC-limited regime increased markedly after 2013 in BTH, FWP, and PRD, by +8.6%, +6.7%, and +13.0%, respectively. For the transitional regime, meteorological contributions increased in all urban clusters except YRD, accompanied by corresponding declines in emission-related contributions of approximately 2.0%–7.3%.

From an overall perspective (Fig. 8d), the relative contribution of emission-related factors decreased slightly after 2013 in BTH, FWP, SCB, and PRD, by about 2.0%–5.6%. In YRD, the relative contributions of meteorological and emission-related factors remained broadly compara-

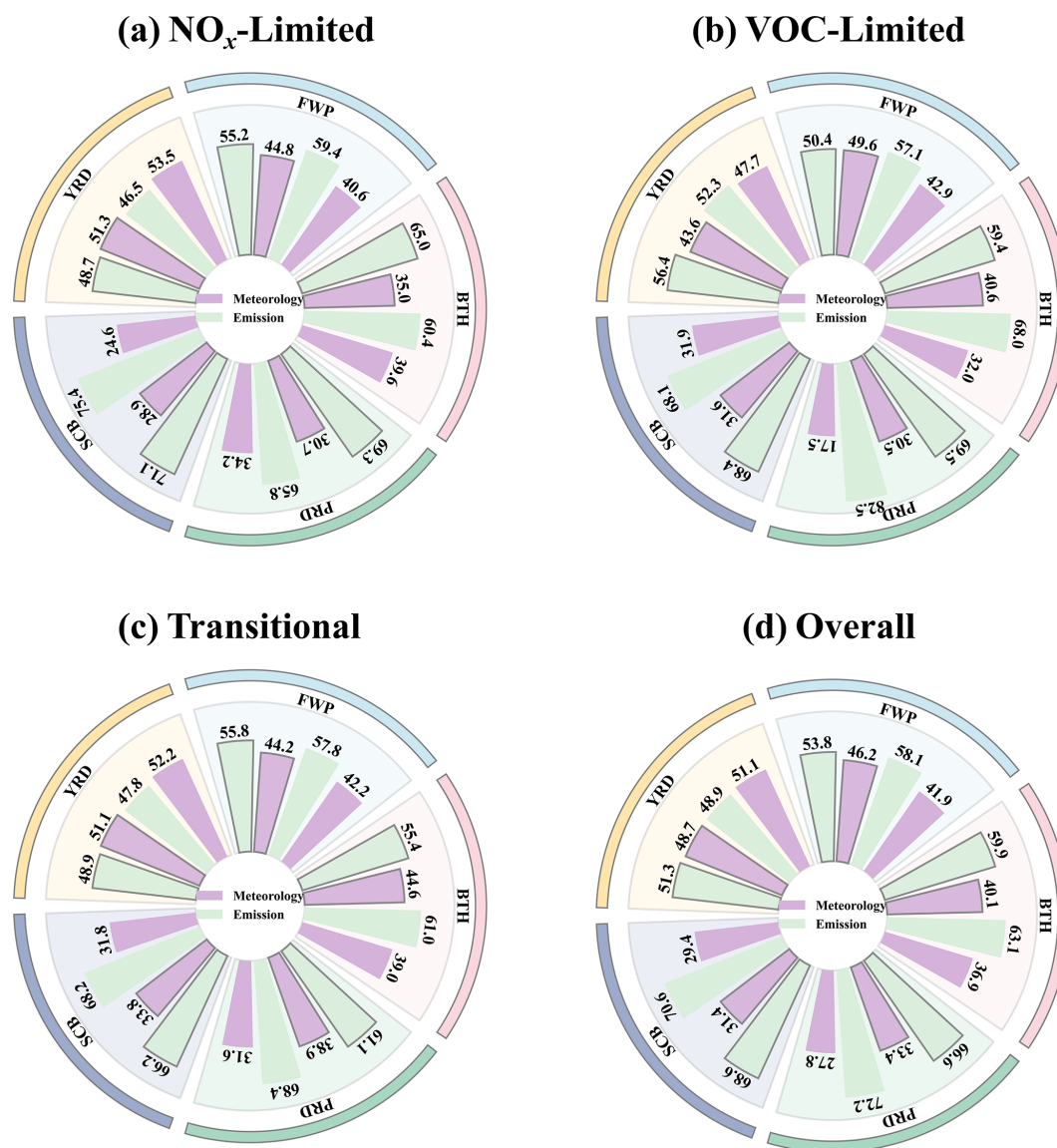


**Figure 8.** Relative contributions (%) of emission-related and meteorological factors to OFS classification in five urban clusters during the warm season (April–September) for the periods of 2005–2012 and 2013–2023, shown separately for (a) NO<sub>x</sub>-limited, (b) VOC-limited, (c) transitional, and (d) overall OFS states. Gray outlined bars denote 2013–2023, whereas bars without outlines denote 2005–2012.

ble, although the balance shifted slightly toward emission-related influences after 2013. Taken together, these results indicate that, while OFS classification remained predominantly emission-driven, the regulatory role of meteorology became more pronounced after 2013. This pattern suggests a modest transition from a regime controlled mainly by emissions toward one jointly modulated by emissions and meteorological conditions. Such a shift is consistent with the substantial reduction in precursor emissions after 2013 and implies that, under a cleaner emission background (Fig. S5), OFS classification may become increasingly sensitive to meteorological variability.

These findings are broadly consistent with previous regional studies, while also highlighting the strong spatial heterogeneity of OFS influencing factors across China. In the Guangdong–Hong Kong–Macao Greater Bay Area, FNR has been reported to be mainly influenced by temperature, shortwave radiation, total column water, and surface pressure (Chen et al., 2020), whereas in Guangdong Province it is primarily associated with surface solar radiation, relative humidity, and temperature (Liang et al., 2024b), although emission-related variables were not explicitly considered. By contrast, in the Chengdu–Chongqing region, summer OFS has been shown to be mainly driven by CO, PM<sub>2.5</sub>, NMVOCs, and NO<sub>x</sub> emissions, with increasing pollution

shifting OFS toward VOC-limited regimes (Xu et al., 2025). In the North China Plain, the decline in  $\text{PM}_{2.5}$  concentrations reduces the loss of  $\text{HO}_2$ , enhances their reaction with  $\text{NO}$ , thereby strengthening  $\text{NO}_x$  sensitivity and leading to increased  $\text{O}_3$  levels (Li et al., 2019). Together, these studies support the view that OFS evolution reflects the combined influence of emissions and meteorology, but that their relative roles differ substantially among regions. Compared with these regional analyses, our results provide a unified national-scale framework showing that emission-related factors generally dominate OFS classification, while meteorological modulation becomes more evident under a cleaner emission background.

#### 3.4.4 SHAP responses of individual predictors across OFS regimes

To further interpret how individual predictors influence OFS classification, we examined the SHAP value distributions of different variables for each urban cluster (Fig. 9). The results reveal both common features and regional differences in the directional and nonlinear effects of the predictors. In general, many variables show broadly opposite SHAP responses between VOC-limited and  $\text{NO}_x$ -limited regimes, indicating that the same predictor can exert contrasting effects under different chemical sensitivity conditions.

For emission-related variables, samples classified as  $\text{NO}_x$ -limited are generally associated with relatively low emission levels. By contrast, under VOC-limited regimes, higher emission values are more consistently associated with positive SHAP values, indicating a greater probability of being classified as VOC-limited. This pattern is broadly consistent with the spatial distribution of OFS, in which  $\text{NO}_x$ -limited regimes are more common in suburban or peripheral areas, whereas VOC-limited regimes are concentrated in urban cores with stronger anthropogenic emissions (Xue et al., 2014; Wang et al., 2021; Johnson et al., 2024). Overall, the regional differences in the SHAP responses of emission variables likely reflect differences in local emission intensity and chemical sensitivity.

Meteorological variables also show substantial but regionally distinct effects on OFS classification. SP, RH, and T emerge as influential predictors in several regions, but their directional effects vary geographically. In BTH and YRD, higher temperatures are more closely associated with  $\text{NO}_x$ -limited classification, which may reflect enhanced photochemical activity and BVOCs emissions under warm conditions (Pétron et al., 2001; Duncan et al., 2009). In several other regions, however, higher temperature is more often linked to VOC-limited classification, which may also be related to the spatial distribution of urban heat islands (Zhou et al., 2015). SP influences pollutant accumulation and vertical mixing through atmospheric stability and subsidence; in general, higher SP favors VOC-limited classification, whereas lower SP is more closely associated with

$\text{NO}_x$ -limited regimes, with particularly asymmetric SHAP responses in YRD. RH is especially important in BTH and YRD, where high humidity tends to promote VOC-limited classification. Higher relative humidity may promote aerosol growth, thereby reducing the radiation reaching the surface and limiting the photochemical production of HCHO (Ye et al., 2016).

Compared with VOC-limited and  $\text{NO}_x$ -limited regimes, the transitional regime shows less consistent directional responses across variables and regions. This suggests that transitional regimes are governed by a more complex combination of emissions and meteorological influences, with stronger nonlinearity and greater classification uncertainty. Such complexity implies that transitional regimes may be the most difficult to manage using simple precursor-reduction strategies alone and may require more detailed process-based analysis to support effective control design.

Overall, the SHAP analysis highlights that OFS classification is shaped by both shared and region-specific predictor responses. Emission-related variables remain the dominant contributors in most regions, whereas meteorological variables modulate the OFS transitions in a region-dependent manner. These results provide a more process-informed interpretation of the regional heterogeneity and temporal evolution of OFS across China during the warm season.

## 4 Conclusion

This study developed an observation-constrained and interpretable framework to diagnose the long-term evolution of OFS across China during the warm season (April–September) from 2005 to 2023. By combining OMI observations of  $\text{NO}_2$  and HCHO with ground-based  $\text{O}_3$  measurements, we derived region-specific FNR threshold ranges and used them to characterize the spatial and temporal evolution of OFS. We further coupled RF models and SHAP analyses to quantify the relative roles of emission-related and meteorological factors in OFS classification.

The long-term evolution of  $\text{O}_3$  precursors showed a pronounced divergence after 2013:  $\text{NO}_2$  declined substantially under strengthened emission-control policies, whereas HCHO continued to increase in many regions. This asynchronous evolution substantially reshaped FNR and provided the precursor basis for subsequent OFS shifts. At the same time, the derived FNR threshold ranges differed markedly across regions, demonstrating that a uniform national threshold is insufficient for OFS diagnosis in China, and that region-specific thresholds provide a more robust basis for reducing classification uncertainty.

Against this background, OFS over China exhibited a clear phase-dependent evolution. During 2005–2012, many regions shifted from  $\text{NO}_x$ -limited toward transitional or VOC-limited regimes as  $\text{NO}_2$  increased. After 2013, the sharp decline in  $\text{NO}_2$  together with a modest rise in HCHO drove a

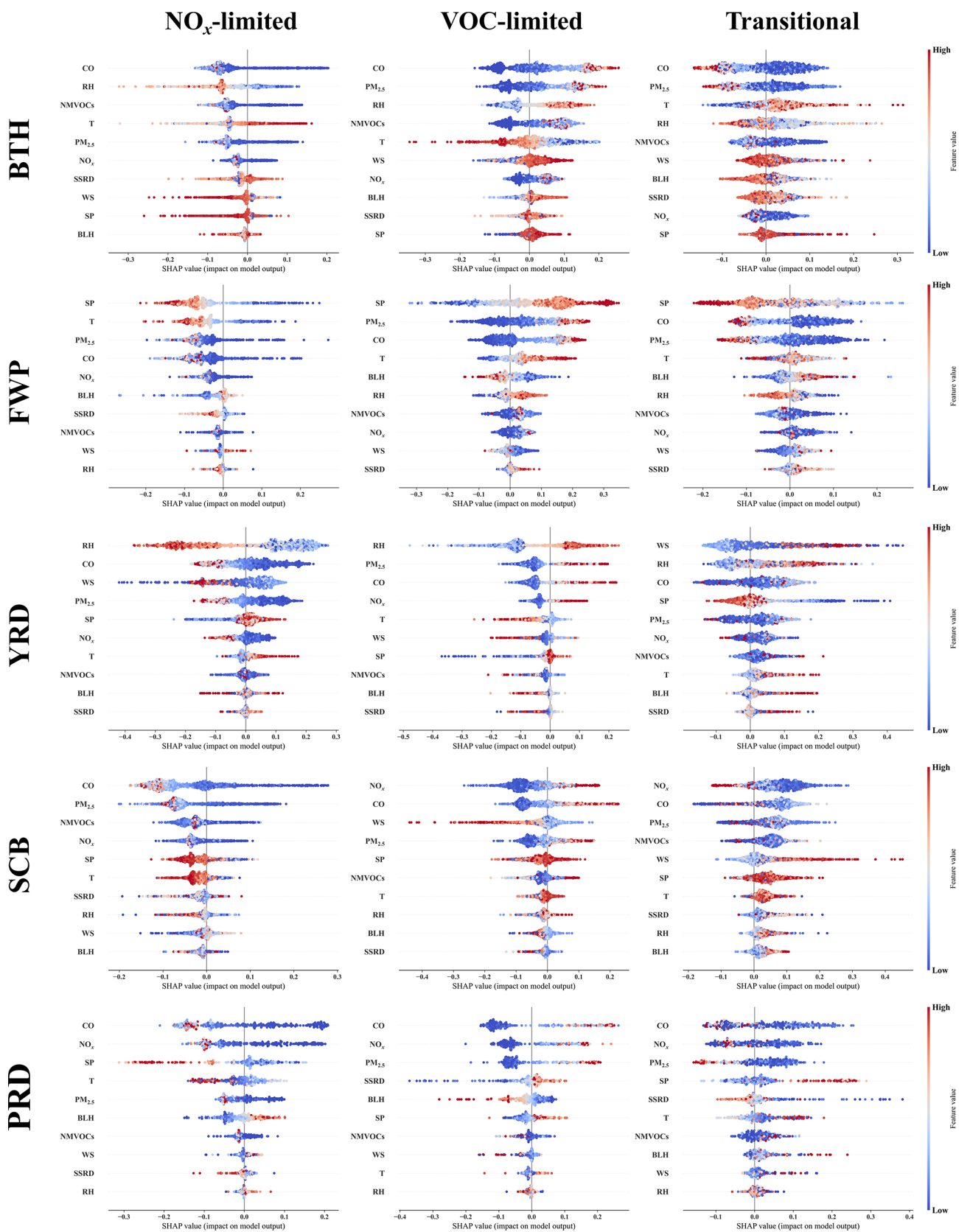


Figure 9. SHAP value distributions of individual predictors in the RF models for the five urban clusters in China.

widespread return toward more  $\text{NO}_x$ -limited chemistry, especially in eastern China. However, this transition was not spatially uniform and exhibited a clear temporal shift around 2013, with BTH and FWP shifting from VOC-limited toward transitional regimes, and YRD evolving toward  $\text{NO}_x$ -limited regimes. SCB remained in largely transitional regimes, while PRD shifted from transitional toward  $\text{NO}_x$ -limited regimes. These results indicate that OFS in China has undergone a policy-related but regionally heterogeneous restructuring over the past two decades.

Although the definition of OFS is based on the relative proportions of precursors, its spatiotemporal patterns actually reflect the combined effects of emission sources and meteorological conditions. Therefore, we treat OFS types as integrated response states and apply ML techniques to statistically model their relationships with meteorological parameters and emission variables. Within this framework, meteorological factors indirectly influence the formation of OFS by modulating the probabilities of different OFS states, rather than directly altering the FNR definition itself. Our focus is on the FNR-derived OFS, rather than absolute  $\text{O}_3$  concentrations, enabling us to elucidate how meteorology governs the classification and evolution of sensitivity regimes. It should be noted that the attribution analysis presented here is based on statistical associations, and the results only reflect the relative contributions of each variable to OFS states, without implying strict causal relationships.

The explainable ML analysis further showed that emission-related variables remained the dominant predictors of OFS classification in most regions, whereas meteorological factors exerted region-dependent modulation of the direction and strength of OFS transitions. After 2013, the relative influence of meteorology increased modestly in several regions, suggesting that under a cleaner emission background, OFS becomes more sensitive to meteorological variability. Overall, these findings indicate that the long-term evolution of OFS in China is primarily driven by emission changes but increasingly modulated by meteorological conditions.

This study is subject to several uncertainties and limitations. First, this is an exploratory application of a classification model to OFS states, and the performance of the RF depends on class balance; however, the threshold-based classification leads to class imbalance, and some influencing factors are not included. Second, the thresholds themselves are uncertain, and the coarse spatial resolution of OMI data, along with mismatches with ground observations, may introduce classification uncertainty and affect model performance. The use of higher-resolution data such as TROPOMI, combined with  $\text{O}_3$  observations, can improve diagnostic accuracy (Ren et al., 2022). Future work integrating ML with observations and chemical transport models may help bridge this gap (Xiong et al., 2024). Therefore, the present framework should be viewed as a complementary statistical attribution tool, rather than a substitute for process-based OFS

diagnosis using chemical transport models or observation-based box models.

In summary, this study derived region-specific FNR threshold ranges and revealed pronounced spatial differences in OFS classification across China, providing a more robust basis for refined  $\text{O}_3$  control. The results further show that the long-term evolution of OFS is primarily shaped by emission changes, while regional meteorological conditions increasingly modulate its spatial distribution and temporal transitions under a cleaner emission background. These findings indicate that future OFS assessments and control strategies should account not only for precursor reductions, but also for regional meteorological variability and the coupled interactions among  $\text{NO}_x$ , NMVOCs,  $\text{PM}_{2.5}$ , and CO. Overall, the satellite–indicator (FNR)–interpretable machine learning (RF + SHAP) framework developed here provides a scalable and decomposable framework for interpreting the long-term evolution and associated factors influencing FNR-derived OFS states from national to urban-cluster scales. This framework offers a useful scientific basis for dynamic sensitivity reclassification and the design of region-specific  $\text{NO}_x$ –VOC control strategies, with broader relevance for  $\text{O}_3$  mitigation in other megacity regions.

**Data availability.** The surface  $\text{O}_3$  network data are available at <https://softnet.air> (last access: 1 February 2026). OMI  $\text{NO}_2$  and HCHO columns for 2005–2023 were obtained from the NASA Goddard Earth Sciences Data and Information Services Center, using the OMNO2d (Krotkov et al., 2019; <https://doi.org/10.5067/Aura/OMI/DATA3007>) and OMIHCHOd (Chance, 2019; <https://doi.org/10.5067/Aura/OMI/DATA3010>). Meteorological data were obtained from the ERA5 reanalysis provided by ECMWF via the Copernicus Climate Data Store (Hersbach et al., 2020; <https://cds.climate.copernicus.eu/>, last access: 6 September 2025). Anthropogenic emissions over China were derived from the Multi-resolution Emission Inventory for China (MEIC; Li et al., 2017; <http://www.meicmodel.org/>, last access: 6 September 2025). Specifically, we used the ERA5 monthly averaged data on pressure levels (Hersbach et al., 2023a, <https://doi.org/10.24381/cds.6860a573>) and ERA5 monthly averaged data on single levels (Hersbach et al., 2023b, <https://doi.org/10.24381/cds.f17050d7>). All datasets were consistently regridded to a  $0.25^\circ \times 0.25^\circ$  spatial resolution for this analysis.

**Supplement.** The supplement related to this article is available online at <https://doi.org/10.5194/acp-26-7081-2026-supplement>.

**Author contributions.** JL, LW and WC designed the research. JL did the data analysis and machine learning work and prepared the draft with support and editing from WC and LW. YW and CC contributed to data analysis. RL and XW contributed to paper revision.

**Competing interests.** The contact author has declared that none of the authors has any competing interests.

**Disclaimer.** Publisher's note: Copernicus Publications remains neutral with regard to jurisdictional claims made in the text, published maps, institutional affiliations, or any other geographical representation in this paper. The authors bear the ultimate responsibility for providing appropriate place names. Views expressed in the text are those of the authors and do not necessarily reflect the views of the publisher.

**Acknowledgements.** The authors are grateful to the editors and anonymous reviewers for their valuable time and insightful comments.

**Financial support.** This study was supported by the National Natural Science Foundation of China (42375109, 42405103), the National Key Research and Development Program of China (2024YFC3714200), the Youth S&T Talent Support Programme of Guangdong Provincial Association for Science and Technology (SKXRC2025350), and the Guangdong Basic and Applied Basic Research Foundation (2023A1515110527).

**Review statement.** This paper was edited by Zhonghua Zheng and reviewed by two anonymous referees.

## References

- Ahmed, A. N., Van Thieu, N., Chong, K. L., Huang, Y. F., and El-Shafie, A.: A comparative analysis of machine learning models for simulating, classifying, and assessment river inflow, *Water Resour. Manage.*, 39, 4051–4069, <https://doi.org/10.1007/s11269-025-04146-1>, 2025.
- Badia, A., Vidal, V., Ventura, S., Curcoll, R., Segura, R., and Vilalba, G.: Modelling the impacts of emission changes on O<sub>3</sub> sensitivity, atmospheric oxidation capacity, and pollution transport over the Catalonia region, *Atmos. Chem. Phys.*, 23, 10751–10774, <https://doi.org/10.5194/acp-23-10751-2023>, 2023.
- Bai, J., de Leeuw, G., van der A, R., De Smedt, I., Theys, N., Van Roozendaal, M., Sogacheva, L., and Chai, W.: Variations and photochemical transformations of atmospheric constituents in North China, *Atmos. Environ.*, 189, 213–226, <https://doi.org/10.1016/j.atmosenv.2018.07.004>, 2018.
- Baruah, U. D., Robeson, S. M., Saikia, A., Mili, N., Sung, K., and Chand, P.: Spatio-temporal characterization of tropospheric ozone and its precursor pollutants NO<sub>2</sub> and HCHO over South Asia, *Sci. Total Environ.*, 809, 151135, <https://doi.org/10.1016/j.scitotenv.2021.151135>, 2022.
- Bauwens, M., Verreyken, B., Stavrou, T., Müller, J. F., and Smedt, I. D.: Spaceborne evidence for significant anthropogenic VOC trends in Asian cities over 2005–2019, *Environ. Res. Lett.*, 17, 015008, <https://doi.org/10.1088/1748-9326/ac46eb>, 2022.
- Bian, Y., Huang, Z., Ou, J., Zhong, Z., Xu, Y., Zhang, Z., Xiao, X., Ye, X., Wu, Y., Yin, X., Li, C., Chen, L., Shao, M., and Zheng, J.: Evolution of anthropogenic air pollutant emissions in Guangdong Province, China, from 2006 to 2015, *Atmos. Chem. Phys.*, 19, 11701–11719, <https://doi.org/10.5194/acp-19-11701-2019>, 2019.
- Breiman, L.: Bagging Predictors, *Mach. Learn.*, 24, 123–140, <https://doi.org/10.1023/A:1018054314350>, 1996.
- Breiman, L.: Random Forests, *Mach. Learn.*, 45, 5–32, <https://doi.org/10.1023/A:1010933404324>, 2001.
- Chance, K.: OMI/Aura Formaldehyde (HCHO) Total Column Daily L3 Weighted Mean Global 0.1deg Lat/Lon Grid V003, Goddard Earth Sciences Data and Information Services Center (GES DISC) [data set], Greenbelt, MD, USA, <https://doi.org/10.5067/Aura/OMI/DATA3010>, 2019.
- Chen, N., Yang, Y., Wang, D., You, J., Gao, Y., Zhang, L., Zeng, Z., and Hu, B.: Changing ozone sensitivity in Fujian Province, China, during 2012–2021: Importance of controlling VOC emissions, *Environ. Pollut.*, 359, 124757, <https://doi.org/10.1016/j.envpol.2024.124757>, 2024.
- Chen, Y., Yan, H., Yao, Y., Zeng, C., Gao, P., Zhuang, L., Fan, L., and Ye, D.: Relationships of ozone formation sensitivity with precursors emissions, meteorology and land use types, in Guangdong-Hong Kong-Macao Greater Bay Area, China, *J. Environ. Sci.*, 94, 1–13, <https://doi.org/10.1016/j.jes.2020.04.005>, 2020.
- Chen, Y., Han, H., Zhang, M., Zhao, Y., Huang, Y., Zhou, M., Wang, C., He, G., Huang, R., Luo, B., and Hu, Y.: Trends and variability of ozone pollution over the mountain-basin areas in Sichuan Province during 2013–2020: Synoptic impacts and formation regimes, *Atmosphere*, 12, 1557, <https://doi.org/10.3390/atmos12121557>, 2021.
- Chen, Y., Wang, M., Yao, Y., Zeng, C., Zhang, W., Yan, H., Gao, P., Fan, L., and Ye, D.: Research on the ozone formation sensitivity indicator of four urban agglomerations of China using Ozone Monitoring Instrument (OMI) satellite data and ground-based measurements, *Sci. Total Environ.*, 869, 161679, <https://doi.org/10.1016/j.scitotenv.2023.161679>, 2023.
- Chinese State Council: Action plan on air pollution prevention and control, [http://www.gov.cn/zwqk/2013-09/12/content\\_2486773.htm](http://www.gov.cn/zwqk/2013-09/12/content_2486773.htm) (last access: 6 November 2025), 2013 (in Chinese).
- Chinese State Council: Three-year action plan on defending the blue sky, [http://www.gov.cn/zhengce/content/2018-07/03/content\\_5303158.htm](http://www.gov.cn/zhengce/content/2018-07/03/content_5303158.htm) (last access: 6 November 2025), 2018 (in Chinese).
- Deng, C., Tian, S., Li, Z., and Li, K.: Spatiotemporal characteristics of PM<sub>2.5</sub> and ozone concentrations in Chinese urban clusters, *Chemosphere*, 295, 133813, <https://doi.org/10.1016/j.chemosphere.2022.133813>, 2022.
- Du, X., Tang, W., Cheng, M., Zhang, Z., Li, Y., Li, Y., and Meng, F.: Modeling of spatial and temporal variations of ozone–NO<sub>x</sub>–VOC sensitivity based on photochemical indicators in China, *J. Environ. Sci.*, 114, 454–464, <https://doi.org/10.1016/j.jes.2021.12.026>, 2022.
- Duncan, B. N., Yoshida, Y., Damon, M. R., Douglass, A. R., and Witte, J. C.: Temperature dependence of factors controlling isoprene emissions, *Geophys. Res. Lett.*, 36, L05813, <https://doi.org/10.1029/2008GL037090>, 2009.
- Duncan, B. N., Yoshida, Y., Olson, J. R., Sillman, S., Martin, R. V., Lamsal, L., Hu, Y., Pickering, K. E., Retscher, C., Allen, D. J., and Crawford, J. H.: Application of OMI obser-

- vations to a space-based indicator of NO<sub>x</sub> and VOC controls on surface ozone formation, *Atmos. Environ.*, 44, 2213–2223, <https://doi.org/10.1016/j.atmosenv.2010.03.010>, 2010.
- Fang, J., Zhang, Y., Hauglustaine, D., Zheng, B., Wang, M., Li, J., Sun, Y., Li, H., Wang, J., Wu, Y., Yuan, B., Chen, M., and Ge, X.: Tracking surface ozone responses to clean air actions under a warming climate in China using machine learning, *Atmos. Chem. Phys.*, 26, 851–867, <https://doi.org/10.5194/acp-26-851-2026>, 2026.
- Feng, X., Li, Q., Zhu, Y., Wang, J., Liang, H., and Xu, R.: Formation and dominant factors of haze pollution over Beijing and its peripheral areas in winter, *Atmos. Pollut. Res.*, 5, 528–538, <https://doi.org/10.5094/APR.2014.062>, 2014.
- Fernandez, A., Garcia, S., Herrera, F., and Chawla, N. V.: SMOTE for learning from imbalanced data: Progress and challenges, marking the 15-year anniversary, *J. Artif. Intell. Res.*, 61, 863–905, <https://doi.org/10.1613/jair.1.11192>, 2018.
- Fu, Y., Sun, W., Fan, D., Zhang, Z., and Hao, Y.: An assessment of China's industrial emission characteristics using satellite observations of XCO<sub>2</sub>, SO<sub>2</sub>, and NO<sub>2</sub>, *Atmos. Pollut. Res.*, 13, 101486, <https://doi.org/10.1016/j.apr.2022.101486>, 2022.
- Geng, G., Liu, Y., Liu, Y., Liu, S., Cheng, J., Yan, L., Wu, N., Hu, H., Tong, D., Zheng, B., Yin, Z., He, K., and Zhang, Q.: Efficacy of China's clean air actions to tackle PM<sub>2.5</sub> pollution between 2013 and 2020, *Nat. Geosci.*, 17, 987–994, <https://doi.org/10.1038/s41561-024-01540-z>, 2024.
- González Abad, G., Liu, X., Chance, K., Wang, H., Kurosu, T. P., and Suleiman, R.: Updated Smithsonian Astrophysical Observatory Ozone Monitoring Instrument (SAO OMI) formaldehyde retrieval, *Atmos. Meas. Tech.*, 8, 19–32, <https://doi.org/10.5194/amt-8-19-2015>, 2015.
- Guan, Y., Xiao, Y., Rong, B., Zhang, N., and Chu, C.: Long-term health impacts attributable to PM<sub>2.5</sub> and ozone pollution in China's most polluted region during 2015–2020, *J. Clean Prod.*, 321, 128970, <https://doi.org/10.1016/j.jclepro.2021.128970>, 2021.
- Hastie, T., Tibshirani, R., and Friedman, J.: Model Assessment and Selection, in: *The Elements of Statistical Learning*, Springer Series in Statistics, Springer, New York, NY, 219–259, [https://doi.org/10.1007/978-0-387-84858-7\\_7](https://doi.org/10.1007/978-0-387-84858-7_7), 2009.
- Hersbach, H., Bell, B., Berrisford, P., Hirahara, S., Horányi, A., Muñoz-Sabater, J., Nicolas, J., Peubey, C., Radu, R., Schepers, D., Simmons, A., Soci, C., Abdalla, S., Abellan, X., Balsamo, G., Bechtold, P., Biavati, G., Bidlot, J., Bonavita, M., De Chiara, G., Dahlgren, P., Dee, D., Diamantakis, M., Dragani, R., Flemming, J., Forbes, R., Fuentes, M., Geer, A., Haimberger, L., Healy, S., Hogan, R. J., Hólm, E., Janisková, M., Keeley, S., Laloyaux, P., Lopez, P., Lupu, C., Radnoti, G., de Rosnay, P., Rozum, I., Vamborg, F., Villaume, S., and Thépaut, J.-N.: The ERA5 global reanalysis, *Q.J.R. Meteorol. Soc.*, 146, 1999–2049, <https://doi.org/10.1002/qj.3803>, 2020.
- Hersbach, H., Bell, B., Berrisford, P., Biavati, G., Horányi, A., Muñoz Sabater, J., Nicolas, J., Peubey, C., Radu, R., Rozum, I., Schepers, D., Simmons, A., Soci, C., Dee, D., and Thépaut, J.-N.: ERA5 monthly averaged data on single levels from 1940 to present, Copernicus Climate Change Service (C3S) Climate Data Store (CDS) [data set], Reading, UK, <https://doi.org/10.24381/cds.6860a573>, 2023a.
- Hersbach, H., Bell, B., Berrisford, P., Biavati, G., Horányi, A., Muñoz Sabater, J., Nicolas, J., Peubey, C., Radu, R., Rozum, I., Schepers, D., Simmons, A., Soci, C., Dee, D., and Thépaut, J.-N.: ERA5 monthly averaged data on single levels from 1940 to present, Copernicus Climate Change Service (C3S) Climate Data Store (CDS) [data set], Reading, UK, <https://doi.org/10.24381/cds.f17050d7>, 2023b.
- Hirsch, R. M., Slack, J. R., and Smith, R. A.: Techniques of trend analysis for monthly water quality data, *Water Resour. Res.*, 18, 107–121, <https://doi.org/10.1029/WR018i001p00107>, 1982.
- Hu, T., Lin, Y., Liu, R., Xu, Y., Ouyang, S., Wang, B., Zhang, Y., and Liu, S. C.: What caused large ozone variabilities in three megacity clusters in eastern China during 2015–2020?, *Atmos. Chem. Phys.*, 24, 1607–1626, <https://doi.org/10.5194/acp-24-1607-2024>, 2024.
- Hua, Q., Meng, X., Chen, W., Xu, Y., Xu, R., Shi, Y., Li, J., Meng, X., Li, A., Chai, Q., Sheng, M., Yao, Y., Fan, Y., Qiao, R., Zhang, Y., Wang, T., Zhang, Y., Cui, X., Yu, Y., Li, H., Tang, R., Yan, M., Duo, B., Dunzhu, D., Ga, Z., Hou, L., Liu, Y., Shang, J., Chen, Q., Qiu, X., Ye, C., Gong, J., and Zhu, T.: Associations of short-term ozone exposure with hypoxia and arterial stiffness, *J. Am. Coll. Cardiol.*, 85, 606–621, <https://doi.org/10.1016/j.jacc.2024.11.044>, 2025.
- Itahashi, S., Irie, H., Shimadera, H., and Chatani, S.: Fifteen-Year trends (2005–2019) in the satellite-derived ozone-sensitive regime in East Asia: A gradual shift from VOC-sensitive to NO<sub>x</sub>-sensitive, *Remote Sens.*, 14, 4512, <https://doi.org/10.3390/rs14184512>, 2022.
- Jin, X. and Holloway, T.: Spatial and temporal variability of ozone sensitivity over China observed from the Ozone Monitoring Instrument, *J. Geophys. Res.-Atmos.*, 120, 7229–7246, <https://doi.org/10.1002/2015JD023250>, 2015.
- Jin, X., Fiore, A., Boersma, K. F., Smedt, I. D., and Valin, L.: Inferring changes in summertime surface ozone–NO<sub>x</sub>–VOC chemistry over U.S. urban areas from two decades of satellite and ground-based observations, *Environ. Sci. Technol.*, 54, 6518–6529, <https://doi.org/10.1021/acs.est.9b07785>, 2020.
- Johnson, M. S., Philip, S., Meech, S., Kumar, R., Sorek-Hamer, M., Shiga, Y. P., and Jung, J.: Insights into the long-term (2005–2021) spatiotemporal evolution of summer ozone production sensitivity in the Northern Hemisphere derived with the Ozone Monitoring Instrument (OMI), *Atmos. Chem. Phys.*, 24, 10363–10384, <https://doi.org/10.5194/acp-24-10363-2024>, 2024.
- Kleinman, L. I.: Low and high NO<sub>x</sub> tropospheric photochemistry, *J. Geophys. Res.-Atmos.*, 99, 16831–16838, <https://doi.org/10.1029/94JD01028>, 1994.
- Koukouli, M. E., Balis, D. S., van der A, R. J., Theys, N., Hedelt, P., Richter, A., Krotkov, N., Li, C., and Taylor, M.: Anthropogenic sulphur dioxide load over China as observed from different satellite sensors, *Atmos. Environ.*, 145, 45–59, <https://doi.org/10.1016/j.atmosenv.2016.09.007>, 2016.
- Krotkov, N. A., Lamsal, L. N., Marchenko, S. V., Celarier, E. A., Bucsela, E. J., Swartz, W. H., Joiner, J., and the OMI core team: OMI/Aura NO<sub>2</sub> Cloud-Screened Total and Tropospheric Column L3 Global Gridded 0.25 degree × 0.25 degree V3, NASA Goddard Space Flight Center, Goddard Earth Sciences Data and Information Services Center (GES DISC) [data set], Greenbelt, MD, USA, <https://doi.org/10.5067/Aura/OMI/DATA3007>, 2019.

- Levelt, P. F., Oord, G. H. J. v. d., Dobber, M. R., Mälkki, A., Huib, V., Johan de, V., Stammes, P., Lundell, J. O. V., and Saari, H.: The ozone monitoring instrument, *IEEE T. Geosci. Remote*, 44, 1093–1101, <https://doi.org/10.1109/TGRS.2006.872333>, 2006.
- Li, C., Zhang, Q., Krotkov, N. A., Streets, D. G., He, K., Tsay, S.-C., and Gleason, J. F.: Recent large reduction in sulfur dioxide emissions from Chinese power plants observed by the Ozone Monitoring Instrument, *Geophys. Res. Lett.*, 37, L08807, <https://doi.org/10.1029/2010GL042594>, 2010.
- Li, J., Zhu, K., Chen, C., Huang, Z., Huang, Y., Sha, Q., Zhu, M., Chen, H., and Zheng, J.: Spatiotemporal evolution of anthropogenic emissions and their impact on air pollution in Guangdong Province from 2006 to 2020, *Sustainability*, 17, 4844, <https://doi.org/10.3390/su17114844>, 2025.
- Li, K., Jacob, D. J., Liao, H., Shen, L., Zhang, Q., and Bates, K. H.: Anthropogenic drivers of 2013–2017 trends in summer surface ozone in China, *P. Natl. Acad. Sci. USA*, 116, 422–427, <https://doi.org/10.1073/pnas.1812168116>, 2019.
- Li, K., Jacob, D. J., Shen, L., Lu, X., De Smedt, I., and Liao, H.: Increases in surface ozone pollution in China from 2013 to 2019: anthropogenic and meteorological influences, *Atmos. Chem. Phys.*, 20, 11423–11433, <https://doi.org/10.5194/acp-20-11423-2020>, 2020.
- Li, M., Liu, H., Geng, G., Hong, C., Liu, F., Song, Y., Tong, D., Zheng, B., Cui, H., Man, H., Zhang, Q., and He, K.: Anthropogenic emission inventories in China: a review, *Natl. Sci. Rev.*, 4, 834–866, <https://doi.org/10.1093/nsr/nwx150>, 2017.
- Li, S., Wang, S., Wu, Q., Zhang, Y., Ouyang, D., Zheng, H., Han, L., Qiu, X., Wen, Y., Liu, M., Jiang, Y., Yin, D., Liu, K., Zhao, B., Zhang, S., Wu, Y., and Hao, J.: Emission trends of air pollutants and CO<sub>2</sub> in China from 2005 to 2021, *Earth Syst. Sci. Data*, 15, 2279–2294, <https://doi.org/10.5194/essd-15-2279-2023>, 2023.
- Li, Y., Yu, C., Tao, J., Lu, X., and Chen, L.: Analysis of ozone formation sensitivity in Chinese representative regions using satellite and ground-based Data, *Remote Sens.*, 16, 316, <https://doi.org/10.3390/rs16020316>, 2024.
- Liang, S., Chen, Y., Sun, X., Dong, X., He, G., Pu, Y., Fan, J., Zhong, X., Chen, Z., Lin, Z., Ma, W., and Liu, T.: Long-term exposure to ambient ozone and cardiovascular diseases: Evidence from two national cohort studies in China, *J. Adv. Res.*, 62, 165–173, <https://doi.org/10.1016/j.jare.2023.08.010>, 2024a.
- Liang, Y., Wang, X., Qi, S., Xu, J., and Liu, R.: Sensitivity analysis of ozone generation in Guangdong Province based on OMI satellite and ground observation data, *Environ. Sci.*, 45, 6248–6254, <https://doi.org/10.13227/j.hjxk.202311261>, 2024b (in Chinese).
- Lin, Y., Jiang, F., Zhao, J., Zhu, G., He, X., Ma, X., Li, S., Sabel, C. E., and Wang, H.: Impacts of O<sub>3</sub> on premature mortality and crop yield loss across China, *Atmos. Environ.*, 194, 41–47, <https://doi.org/10.1016/j.atmosenv.2018.09.024>, 2018.
- Liu, C. and Shi, K.: A review on methodology in O<sub>3</sub>–NO<sub>x</sub>–VOC sensitivity study, *Environ. Pollut.*, 291, 118249, <https://doi.org/10.1016/j.envpol.2021.118249>, 2021.
- Liu, R., Shao, M., and Wang, Q.: Multi-timescale variation characteristics of PM<sub>2.5</sub> in different regions of China during 2014–2022, *Sci. Total Environ.*, 920, 171008, <https://doi.org/10.1016/j.scitotenv.2024.171008>, 2024.
- Lu, X., Hong, J., Zhang, L., Cooper, O. R., Schultz, M. G., Xu, X., Wang, T., Gao, M., Zhao, Y., and Zhang, Y.: Severe surface ozone pollution in China: A global perspective, *Environ. Sci. Technol. Lett.*, 5, 487–494, <https://doi.org/10.1021/acs.estlett.8b00366>, 2018.
- Lu, X., Chen, Y., Huang, Y., Chen, D., Shen, J., Lin, C., Li, Z., Fung, J. C. H., and Lau, A. K. H.: Exposure and mortality apportionment of PM<sub>2.5</sub> between 2006 and 2015 over the Pearl River Delta region in southern China, *Atmos. Environ.*, 231, 117512, <https://doi.org/10.1016/j.atmosenv.2020.117512>, 2020a.
- Lu, X., Zhang, L., Wang, X., Gao, M., Li, K., Zhang, Y., Yue, X., and Zhang, Y.: Rapid increases in warm-season surface ozone and resulting health impact in China since 2013, *Environ. Sci. Technol. Lett.*, 7, 240–247, <https://doi.org/10.1021/acs.estlett.0c00171>, 2020b.
- Lundberg, S. M. and Lee, S.-I.: A unified approach to interpreting model predictions, *arXiv [preprint]*, <https://doi.org/10.48550/arXiv.1705.07874>, 2017.
- Luo, Z., Lu, P., Chen, Z., and Liu, R.: Ozone concentration estimation and meteorological impact quantification in the Beijing–Tianjin–Hebei region based on machine learning models, *Earth Space Sci.*, 11, e2023EA003346, <https://doi.org/10.1029/2023EA003346>, 2024.
- Martin, R. V., Fiore, A. M., and Van Donkelaar, A.: Space-based diagnosis of surface ozone sensitivity to anthropogenic emissions, *Geophys. Res. Lett.*, 31, <https://doi.org/10.1029/2004GL019416>, 2004.
- Milford, J. B., Gao, D., Sillman, S., Blossey, P., and Russell, A. G.: Total reactive nitrogen (NO<sub>y</sub>) as an indicator of the sensitivity of ozone to reductions in hydrocarbon and NO<sub>x</sub> emissions, *J. Geophys. Res.*, 99, 3533–3542, <https://doi.org/10.1029/93JD03224>, 1994.
- Ni, Y., Yang, Y., Wang, H., Li, H., Li, M., Wang, P., Li, K., and Liao, H.: Contrasting changes in ozone during 2019–2021 between eastern and the other regions of China attributed to anthropogenic emissions and meteorological conditions, *Sci. Total Environ.*, 908, 168272, <https://doi.org/10.1016/j.scitotenv.2023.168272>, 2024.
- Ozone Pollution Control Committee of Chinese Society of Environmental Sciences: China blue book on prevention and control of atmospheric ozone pollution (2023), Science Press, Chinese mainland, 164 pp., ISBN 9787030781840, 2024.
- Özupak, Y., Alsalaz, F., and Aslan, E.: Air quality forecasting using machine learning: Comparative analysis and ensemble strategies for enhanced prediction, *Water Air Soil Pollut.*, 236, 464, <https://doi.org/10.1007/s11270-025-08122-8>, 2025.
- Pétron, G., Harley, P., Greenberg, J., and Guenther, A.: Seasonal temperature variations influence isoprene emission, *Geophys. Res. Lett.*, 28, 1707–1710, <https://doi.org/10.1029/2000GL011583>, 2001.
- Pettitt, A. N.: A Non-Parametric Approach to the Change-Point Problem, *J.R. Stat. Soc. Ser. C Appl. Stat.*, 28, 126–135, <https://doi.org/10.2307/2346729>, 1979.
- Qiao, J., Liu, X., Ma, Q., Li, Y., and Li, J.: Impact of Covid-19 pandemic on atmospheric environment over China: a satellite perspective, in: Proceedings of IGARSS 2022–2022 IEEE International Geoscience and Remote Sensing Symposium, Kuala Lumpur, Malaysia, 17–22 July 2022, 6614–6617, <https://doi.org/10.1109/IGARSS46834.2022.9884338>, 2022.
- Ren, J., Guo, F., and Xie, S.: Diagnosing ozone–NO<sub>x</sub>–VOC sensitivity and revealing causes of ozone increases in China based on

- 2013–2021 satellite retrievals, *Atmos. Chem. Phys.*, 22, 15035–15047, <https://doi.org/10.5194/acp-22-15035-2022>, 2022.
- Ren, X., van Duin, D., Cazorla, M., Chen, S., Mao, J., Zhang, L., Brune, W. H., Flynn, J. H., Grossberg, N., Lefer, B. L., Rappenglück, B., Wong, K. W., Tsai, C., Stutz, J., Dibb, J. E., Thomas Jobson, B., Luke, W. T., and Kelley, P.: Atmospheric oxidation chemistry and ozone production: Results from SHARP 2009 in Houston, Texas, *J. Geophys. Res.-Atmos.*, 118, 5770–5780, <https://doi.org/10.1002/jgrd.50342>, 2013.
- Sadaiyandi, J., Arumugam, P., Sangaiah, A. K., and Zhang, C.: Stratified sampling-based deep learning approach to increase prediction accuracy of unbalanced dataset, *Electronics*, 12, 4423, <https://doi.org/10.3390/electronics12214423>, 2023.
- Schroeder, J. R., Crawford, J. H., Fried, A., Walega, J., Weinheimer, A., Wisthaler, A., Müller, M., Mikoviny, T., Chen, G., Shook, M., Blake, D. R., and Tonnesen, G. S.: New insights into the column CH<sub>2</sub>O/NO<sub>2</sub> ratio as an indicator of near-surface ozone sensitivity, *J. Geophys. Res.-Atmos.*, 122, 8885–8907, <https://doi.org/10.1002/2017JD026781>, 2017.
- Seinfeld, J. H. and Pandis, S. N.: *Atmospheric Chemistry and Physics*, in: *Air Pollution to Climate Change*, John Wiley & Sons, 1152 pp., ISBN 978-1-118-94740-1, 2016.
- Sen, P. K.: Estimates of the regression coefficient based on Kendall's tau, *J. Am. Stat. Assoc.*, 63, 1379–1389, <https://doi.org/10.1080/01621459.1968.10480934>, 1968.
- Shah, V., Jacob, D. J., Li, K., Silvern, R. F., Zhai, S., Liu, M., Lin, J., and Zhang, Q.: Effect of changing NO<sub>x</sub> lifetime on the seasonality and long-term trends of satellite-observed tropospheric NO<sub>2</sub> columns over China, *Atmos. Chem. Phys.*, 20, 1483–1495, <https://doi.org/10.5194/acp-20-1483-2020>, 2020.
- Sillman, S.: The use of NO<sub>y</sub>, H<sub>2</sub>O<sub>2</sub>, and HNO<sub>3</sub> as indicators for ozone–NO<sub>x</sub>–hydrocarbon sensitivity in urban locations, *J. Geophys. Res.-Atmos.*, 100, 14175–14188, <https://doi.org/10.1029/94JD02953>, 1995.
- Sillman, S.: The relation between ozone, NO<sub>x</sub> and hydrocarbons in urban and polluted rural environments, *Atmos. Environ.*, 33, 1821–1845, [https://doi.org/10.1016/S1352-2310\(98\)00345-8](https://doi.org/10.1016/S1352-2310(98)00345-8), 1999.
- Song, H., Zhao, W., Yang, X., Hou, W., Chen, L., and Ma, P.: Ozone sensitivity analysis and ozone formation regimes division in the Beijing–Tianjin–Hebei region based on satellite remote sensing data, *Atmosphere*, 14, 1637, <https://doi.org/10.3390/atmos14111637>, 2023.
- Stavrakou, T., Müller, J.-F., Bauwens, M., Doumbia, T., Elguindi, N., Darras, S., Granier, C., Smedt, I. D., Lerot, C., Van Roozendael, M., Franco, B., Clarisse, L., Clerbaux, C., Coheur, P.-F., Liu, Y., Wang, T., Shi, X., Gaubert, B., Tilmes, S., and Brasseur, G.: Atmospheric impacts of COVID-19 on NO<sub>x</sub> and VOC levels over China based on TROPOMI and IASI satellite data and modeling, *Atmosphere*, 12, 946, <https://doi.org/10.3390/atmos12080946>, 2021.
- Thieu, N. V.: PerMetrics: A framework of performance metrics for machine learning models, *J. Open Source Softw.*, 9, 6143, <https://doi.org/10.21105/joss.06143>, 2024.
- Tonnesen, G. S. and Dennis, R. L.: Analysis of radical propagation efficiency to assess ozone sensitivity to hydrocarbons and NO<sub>x</sub>: 2. Long-lived species as indicators of ozone concentration sensitivity, *J. Geophys. Res.-Atmos.*, 105, 9227–9241, <https://doi.org/10.1029/1999JD900372>, 2000.
- Vazquez Santiago, J., Hata, H., Martinez-Noriega, E. J., and Inoue, K.: Ozone trends and their sensitivity in global megacities under the warming climate, *Nat. Commun.*, 15, 10236, <https://doi.org/10.1038/s41467-024-54490-w>, 2024.
- Wang, N., Du, Y., Chen, D., Meng, H., Chen, X., Zhou, L., Shi, G., Zhan, Y., Feng, M., Li, W., Chen, M., Li, Z., and Yang, F.: Spatial disparities of ozone pollution in the Sichuan Basin spurred by extreme, hot weather, *Atmos. Chem. Phys.*, 24, 3029–3042, <https://doi.org/10.5194/acp-24-3029-2024>, 2024.
- Wang, S., Ren, Y., and Xia, B.: PM<sub>2.5</sub> and O<sub>3</sub> concentration estimation based on interpretable machine learning, *Atmos. Pollut. Res.*, 14, 101866, <https://doi.org/10.1016/j.apr.2023.101866>, 2023.
- Wang, T., Xue, L., Brimblecombe, P., Lam, Y. F., Li, L., and Zhang, L.: Ozone pollution in China: A review of concentrations, meteorological influences, chemical precursors, and effects, *Sci. Total Environ.*, 575, 1582–1596, <https://doi.org/10.1016/j.scitotenv.2016.10.081>, 2017.
- Wang, W., van der A, R., Ding, J., van Weele, M., and Cheng, T.: Spatial and temporal changes of the ozone sensitivity in China based on satellite and ground-based observations, *Atmos. Chem. Phys.*, 21, 7253–7269, <https://doi.org/10.5194/acp-21-7253-2021>, 2021.
- Wang, W., Parrish, D. D., Wang, S., Bao, F., Ni, R., Li, X., Yang, S., Wang, H., Cheng, Y., and Su, H.: Long-term trend of ozone pollution in China during 2014–2020: distinct seasonal and spatial characteristics and ozone sensitivity, *Atmos. Chem. Phys.*, 22, 8935–8949, <https://doi.org/10.5194/acp-22-8935-2022>, 2022.
- Wei, J., Li, Z., Li, K., Dickerson, R. R., Pinker, R. T., Wang, J., Liu, X., Sun, L., Xue, W., and Cribb, M.: Full-coverage mapping and spatiotemporal variations of ground-level ozone (O<sub>3</sub>) pollution from 2013 to 2020 across China, *Remote Sens. Environ.*, 270, 112775, <https://doi.org/10.1016/j.rse.2021.112775>, 2022.
- Weng, X., Forster, G. L., and Nowack, P.: A machine learning approach to quantify meteorological drivers of ozone pollution in China from 2015 to 2019, *Atmos. Chem. Phys.*, 22, 8385–8402, <https://doi.org/10.5194/acp-22-8385-2022>, 2022.
- Wu, K., Yang, X., Chen, D., Gu, S., Lu, Y., Jiang, Q., Wang, K., Ou, Y., Qian, Y., Shao, P., and Lu, S.: Estimation of biogenic VOC emissions and their corresponding impact on ozone and secondary organic aerosol formation in China, *Atmos. Res.*, 231, 104656, <https://doi.org/10.1016/j.atmosres.2019.104656>, 2020.
- Wu, W., Fu, T.-M., Arnold, S. R., Spracklen, D. V., Zhang, A., Tao, W., Wang, X., Hou, Y., Mo, J., Chen, J., Li, Y., Feng, X., Lin, H., Huang, Z., Zheng, J., Shen, H., Zhu, L., Wang, C., Ye, J., and Yang, X.: Temperature-Dependent evaporative anthropogenic VOC emissions significantly exacerbate regional ozone pollution, *Environ. Sci. Technol.*, 58, 5430–5441, <https://doi.org/10.1021/acs.est.3c09122>, 2024.
- Wu, Y., Chen, W., Yan, F., Mao, J., Yuan, B., Wang, W., and Wang, X.: Nonlinear response relationship between ozone and precursor emissions in the Pearl River Delta region under different transmission channels, *Environ. Sci.*, 43, 160–169, <https://doi.org/10.13227/j.hjxk.202104141>, 2022 (in Chinese).
- Xia, H., Wang, D., Abad, G. G., Yang, X., Zhu, L., Pu, D., Feng, X., Zhang, A., Song, Z., Mo, Y., and Wang, J.: Multi-scale correlation reveals the evolution of socio-natural contributions to tropospheric HCHO over China

- from 2005 to 2022, *Sci. Total Environ.*, 954, 176197, <https://doi.org/10.1016/j.scitotenv.2024.176197>, 2024.
- Xiong, K., Xie, X., Huang, L., and Hu, J.: Improved O<sub>3</sub> predictions in China by combining chemical transport model and multi-source data with machining learning techniques, *Atmos. Environ.*, 318, 120269, <https://doi.org/10.1016/j.atmosenv.2023.120269>, 2024.
- Xu, W., Yang, H., He, M., Yang, Z., Zhang, Y., Liu, Z. H., and He, Y. M.: Spatial and temporal characteristics of ozone formation sensitivity and its influencing factors in Chengdu-Chongqing area, *Environ. Sci.*, 46, 736–745, <https://doi.org/10.13227/j.hjlx.202312065>, 2025 (in Chinese).
- Xue, L. K., Wang, T., Gao, J., Ding, A. J., Zhou, X. H., Blake, D. R., Wang, X. F., Saunders, S. M., Fan, S. J., Zuo, H. C., Zhang, Q. Z., and Wang, W. X.: Ground-level ozone in four Chinese cities: precursors, regional transport and heterogeneous processes, *Atmos. Chem. Phys.*, 14, 13175–13188, <https://doi.org/10.5194/acp-14-13175-2014>, 2014.
- Yao, T., Ye, H., Wang, Y., Zhang, J., Guo, J., and Li, J.: Kolmogorov-Zurbenko filter coupled with machine learning to reveal multiple drivers of surface ozone pollution in China from 2015 to 2022, *Sci. Total Environ.*, 949, 175093, <https://doi.org/10.1016/j.scitotenv.2024.175093>, 2024.
- Ye, X., Song, Y., Cai, X., and Zhang, H.: Study on the synoptic flow patterns and boundary layer process of the severe haze events over the North China Plain in January 2013, *Atmos. Environ.*, 124, 129–145, <https://doi.org/10.1016/j.atmosenv.2015.06.011>, 2016.
- Zeng, J., Zhang, Y., Mu, Z., Pang, W., Zhang, H., Wu, Z., Song, W., and Wang, X.: Temperature and light dependency of isoprene and monoterpene emissions from tropical and subtropical trees: Field observations in south China, *Appl. Geochem.*, 155, 105727, <https://doi.org/10.1016/j.apgeochem.2023.105727>, 2023.
- Zhan, J., Liu, Y., Ma, W., Zhang, X., Wang, X., Bi, F., Zhang, Y., Wu, Z., and Li, H.: Ozone formation sensitivity study using machine learning coupled with the reactivity of volatile organic compound species, *Atmos. Meas. Tech.*, 15, 1511–1520, <https://doi.org/10.5194/amt-15-1511-2022>, 2022.
- Zhang, C., Xie, Y., Shao, M., and Wang, Q.: Application of machine learning to analyze ozone sensitivity to influencing factors: A case study in Nanjing, China, *Sci. Total Environ.*, 929, 172544, <https://doi.org/10.1016/j.scitotenv.2024.172544>, 2024a.
- Zhang, J., Shen, A., Jin, Y., Cui, Y., Xu, Y., Lu, X., Liu, Y., and Fan, Q.: Evolution of ozone formation regimes during different periods in representative regions of China, *Atmos. Environ.*, 338, 120830, <https://doi.org/10.1016/j.atmosenv.2024.120830>, 2024b.
- Zhang, Q., Xue, Z., Yi, L., Wang, J., and Liu, E.: Temperature regulates BVOCs-induced O<sub>3</sub> formation potential across various vegetation types in the Sichuan Basin, China, *Forests*, 16, 1091, <https://doi.org/10.3390/f16071091>, 2025a.
- Zhang, R., Cohan, A., Pour Biazar, A., and Cohan, D. S.: Source apportionment of biogenic contributions to ozone formation over the United States, *Atmos. Environ.*, 164, 8–19, <https://doi.org/10.1016/j.atmosenv.2017.05.044>, 2017.
- Zhang, S., Yuan, Z., Zheng, Z., and Zhao, K.: Quantitative impacts of dominant large-scale circulation systems on surface ozone pollution in China, *J. Environ. Sci.*, 156, 42–55, <https://doi.org/10.1016/j.jes.2024.07.015>, 2025b.
- Zhang, Y. and Song, X.: Techniques of abrupt change detection and trends analysis in hydroclimatic time-series: Advances and evaluation, *Arid Land Geogr.*, 38, 652–665, <https://doi.org/10.13826/j.cnki.cn65-1103/x.2015.04.002>, 2015 (in Chinese).
- Zhang, Y., Gao, J., Zhu, Y., Liu, Y., Li, H., Yang, X., Zhong, X., Zhao, M., Wang, W., Che, F., Zhou, D., Wang, S., Zhi, G., Xue, L., and Li, H.: Evolution of ozone formation sensitivity during a persistent regional ozone episode in Northeastern China and its implication for a control strategy, *Environ. Sci. Technol.*, 58, 617–627, <https://doi.org/10.1021/acs.est.3c03884>, 2024c.
- Zhao, C., Zhang, C., Lin, J., Wang, S., Liu, H., Wu, H., and Liu, C.: Variations of urban NO<sub>2</sub> pollution during the COVID-19 outbreak and post-epidemic era in China: A synthesis of remote sensing and in situ measurements, *Remote Sens.*, 14, 419, <https://doi.org/10.3390/rs14020419>, 2022.
- Zheng, B., Tong, D., Li, M., Liu, F., Hong, C., Geng, G., Li, H., Li, X., Peng, L., Qi, J., Yan, L., Zhang, Y., Zhao, H., Zheng, Y., He, K., and Zhang, Q.: Trends in China's anthropogenic emissions since 2010 as the consequence of clean air actions, *Atmos. Chem. Phys.*, 18, 14095–14111, <https://doi.org/10.5194/acp-18-14095-2018>, 2018.
- Zhou, D., Zhao, S., Zhang, L., Sun, G., and Liu, Y.: The footprint of urban heat island effect in China, *Sci. Rep.*, 5, 11160, <https://doi.org/10.1038/srep11160>, 2015.
- Zhu, L., Mickley, L. J., Jacob, D. J., Marais, E. A., Sheng, J., Hu, L., Abad, G. G., and Chance, K.: Long-term (2005–2014) trends in formaldehyde (HCHO) columns across North America as seen by the OMI satellite instrument: Evidence of changing emissions of volatile organic compounds, *Geophys. Res. Lett.*, 44, 7079–7086, <https://doi.org/10.1002/2017GL073859>, 2017.